Vol.40 No.3　2016

Journal

Measurement Technique, High-Frequency Devices

Power Magnetics

JOURNAL OF THE MAGNETICS SOCIETY OF JAPAN

*Vol.*40 *No.*3   2016

Journal of the Magnetics Society of Japan
Vol. 40, No. 3

CONTENTS

<Paper>

Effect of Oxidation Protection Layer
on the Performance of Magnetic Force Microscope Tip

Keiichi Kato, Mitsuru Ohtake, Masaaki Futamoto, Fumiyoshi Kirino*, and Nobuyuki Inaba**

Faculty of Science and Engineering, Chuo University, *1-13-27 Kasuga, Bunkyo-ku, Tokyo 112-8551, Japan*
*Graduate School of Fine Arts, Tokyo University of the Arts, *12-8 Ueno-koen, Taito-ku, Tokyo 110-8714, Japan*
**Faculty of Engineering, Yamagata University, *4-3-16 Jyonan, Yonezawa, Yamagata 992-8510, Japan*

Magnetic force microscope (MFM) tips are prepared by coating silicon tips of 4 nm radius with 20-nm-thick metallic magnetic films with and without 2-nm-thick oxidation protection layers. Iron (Fe) is used as the magnetic material, whereas carbon (C), silicon nitride (Si-N), or silicon carbide (Si-C) is employed as the protection layer. The MFM tips are exposed in an environment of high temperature of 70 °C and high relative humidity of nearly 100%. The effect of protection layer on the spatial resolution is investigated as a function of period of exposure to the environment. The resolution of MFM tip without protection layer deteriorates from 7.2 to 21.2 nm in 10 days. The deterioration is attributed to an increase in the tip radius and a loss of the detection sensitivity caused by oxidation of coated Fe material. In contrast, the resolutions of tips with C, Si-N, and Si-C layers are kept almost constant at 12.1 ± 0.5, 12.1 ± 0.5, and 14.8 ± 2.1 nm for a time span of 10 days, respectively. The coating of a very thin protection layer has been shown effective in keeping the MFM tip performance for a long period of time by preventing the oxidation of coated metallic magnetic material.

Key words: magnetic force microscope, tip, spatial resolution, oxidation protection layer

1. Introduction

Magnetic force microscopy (MFM) has been widely used to investigate the nano-scale magnetization structures of magnetic devices like hard disk drive (HDD) media. MFM tip is prepared by coating a non-magnetic sharp tip with a magnetic film and it is the key component which determines the spatial resolution. The areal density of HDD medium is now approaching 1 Tb/in^2, where the bit length is becoming narrower than 30 nm. MFM resolution of around 15 nm or better is thus necessary to observe the magnetization structures of high-end recording media. However, the resolution of commercially available MFM tip is limited at around 20–30 nm. In order to improve the resolution, the tip needs to be sharp so that a very small volume of magnetic material around the top interacts with a magnetic observation sample surface. Various methods such as tip fabrication by focused ion beam etching[1–4], magnetic material deposition on a sharp non-magnetic tip made of silicon (Si)[5] or carbon nanotube[6–8], etc. have been tried. In our previous studies[9–15], MFM tips were prepared by coating Si tips with various magnetic materials like iron (Fe), iron-boron alloy, iron-cobalt alloy, cobalt-platinum ordered alloy, etc. The signal detection sensitivity of MFM tip was improved by coating a material with higher saturation magnetization (M_s). The resolution was influenced not only by the tip radius but also by the detection sensitivity.

MFM tips prepared by coating metallic magnetic materials are expected to oxidize when kept in a normal atmosphere due to chemical reaction with oxygen or water vapor. In this case, the resolution tends to deteriorate because the magnetic sensitivity of MFM tip will decrease depending on the oxidation of coated metallic magnetic material. By applying a thin protection layer to MFM tip, it seems possible to keep a high resolution property for a long period of time.

In the present study, the effect of oxidation protection layer on the MFM performance is investigated by employing Fe-coated MFM tips. Fe-coated tips show high resolution characteristics when tested soon after preparation[9,10,15]. However, it was noted that the resolution deteriorated when the tip was kept under an ambient atmosphere, possibly due to easy oxidation of Fe material. Therefore, it seems useful to employ Fe-coated tips to investigate the effect of thin protection layer on the variation of MFM tip performance as a function of exposure time. The protection layer must be very thin and continuous to keep the distance between the magnetic tip and a sample as small as possible and to prevent oxidation of magnetic material. Carbon (C), silicon nitride (Si-N), and silicon carbide (Si-C) are selected as the protection layer materials. These non-magnetic materials have been studied as the protection layers for magnetic recording media[16] and they are also supposed to work as the protection layers for MFM tips. The variations of resolution as a function of time are compared between MFM tips with and without protection layers.

2. Experimental Procedure

A radio-frequency (RF) magnetron sputtering system with the base pressures lower than 4×10^{-7} Pa was employed for coating. Commercial Si tips with top radius of 4 nm were used as the base tips. Fe, C, Si_3N_4, and SiC targets of 3 inch diameter were used and the respective RF powers were fixed at 48, 300, 190, and 150 W. The distance between target and Si tip was 150
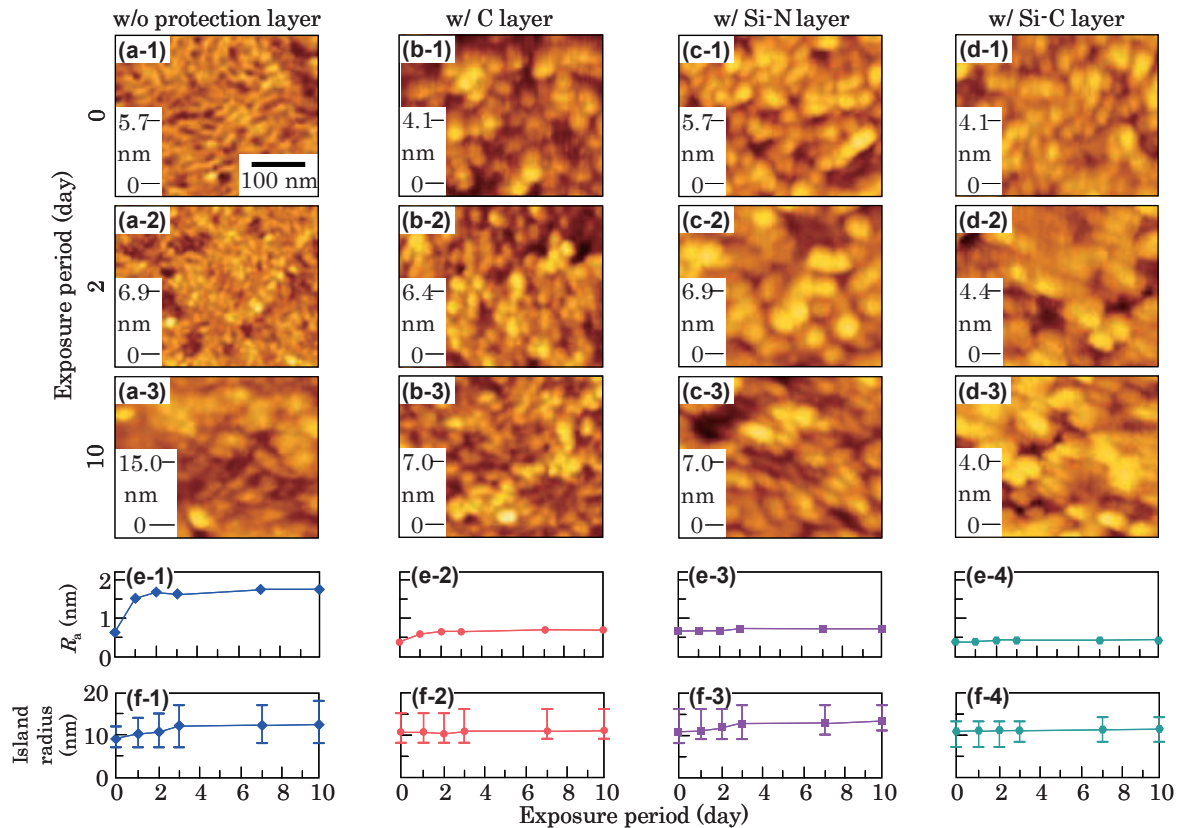
Fig. 1 (a)–(d) AFM images observed for Fe films (a) without and with (b) C, (c) Si-N, and (d) Si-C protection layers deposited on flat Si substrates, (a-1)–(d-1) before and (a-2)–(d-3) after exposure to an environment of 70 °C and nearly 100% relative humidity for (a-2)–(d-2) 2 and (a-3)–(d-3) 10 days. [(e), (f)] Dependences of exposure period on (e) R_a and (f) average island radius.

mm. The Ar gas pressure during sputtering was kept constant at 0.67 Pa. Under the conditions, the deposition rate was 0.020 nm/s for Fe, Si-N, and Si-C materials, while that was 0.017 nm/s for C material. 20-nm-thick Fe films and 2-nm-thick protection layers of C, Si-N, or Si-C were sequentially deposited on Si tips at room temperature (RT). MFM tips without protection layers were also prepared. The coating thicknesses were estimated for films deposited on flat Si substrates, which were located near the base tips in the sputter deposition system. The flat films were also used for structural and magnetic characterizations of coated film materials. The MFM tips and the flat magnetic films were exposed in an environment of 70 °C and nearly 100% relative humidity for acceleration of oxidation up to 10 days. Oxidation rate obeys the Arrhenius Law and the rate (v) is expressed as, $v \propto \exp(-E_a / k_B T)$, where E_a is activation energy, k_B is Boltzmann constant, and T is absolute temperature. The rate is considered to be proportional to the concentration of water vapor, H_2O, humidity. When $E_a = 28$ kJ / mol[17] and T (RT) = 293 K (20 °C), 343 K (70 °C) are employed, the oxidation rate (v) at 70 °C is estimated to be 5.3 times of the rate at RT. When the humidity of ambient atmosphere, around 50%, is considered, the exposure test at 70 °C under 100% relative humidity corresponds to an acceleration of about 10 times. The tip shapes were observed by scanning electron microscopy (SEM). The surface

roughnesses and the magnetic properties of flat films were measured by atomic force microscopy (AFM) and by vibrating sample magnetometry, respectively.

MFM observation was carried out at RT under pressures lower than 0.1 Pa. A perpendicular medium recorded at linear densities ranging from 500 to 1800 kilo flux change per inch (kFCI) was used as an observation sample. MFM tips were magnetized along the tip axis so that the tip top possessed the south magnetic pole. In this case, the bright and the dark contrasts in an MFM image, respectively, correspond to the areas where repulsive and attractive forces are working between the tip and the observation sample. The quality factor value, the distance between tip and observation sample, and the scanning speed were respectively 3000–6000 (dimensionless), 4 ± 1 nm, and 1.4 m/s. The resolutions of MFM tips were carefully determined by optimizing the observation conditions.

3. Results and Discussion

Figures 1(a)–(d) show the AFM images observed for Fe films without and with protection layers deposited on flat Si substrates before and after exposure to the environment of 70 °C and nearly 100% relative humidity. Figures 1(e) and (f) summarize the arithmetical mean surface roughness (R_a) values and the average island radiuses, respectively. Here, the island radius is estimated by using the relation, (radius)
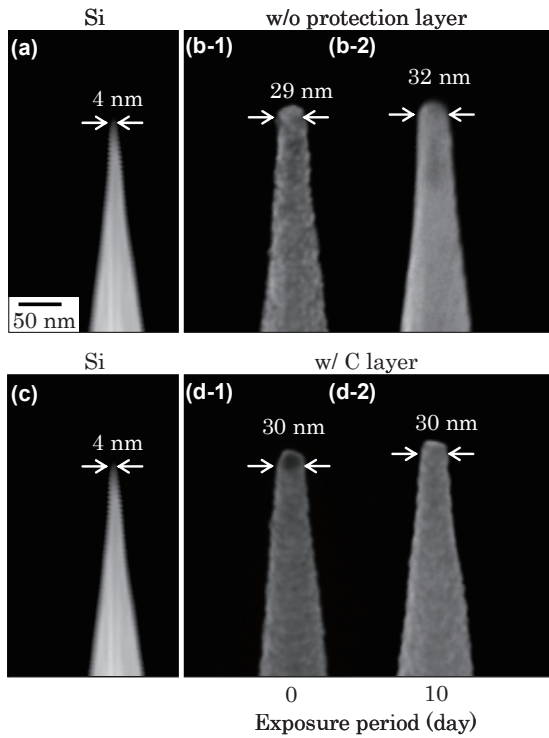
Fig. 2 (a) (c) SEM images of Si tips with 4 nm radius before film coating. (b-1) and (b-2) respectively show the profiles of tip coated with Fe-layer before and after exposure to an environment of 70 °C and nearly 100% relative humidity for 10 days. (d-1) and (d-2) respectively show the profiles of tip coated with Fe-layer and C-protection-layer before and after exposure to the environment for 10 days.
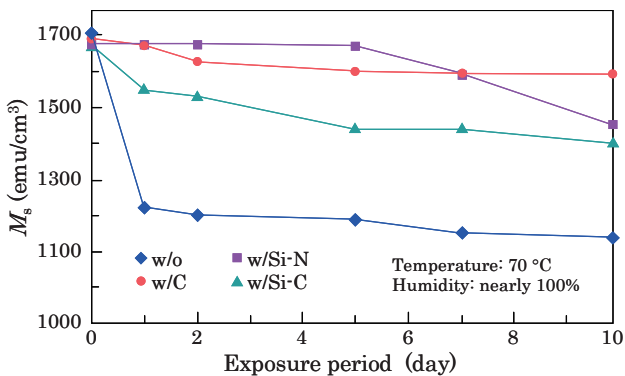

Fig. 3 Dependence of M_s on exposure period measured for Fe films without and with C, Si-N, and Si-C protection layers deposited on flat Si substrates.

Fig. 4 (a) MFM images of a perpendicular medium recorded at (a-1) 500, (a-2) 750, (a-3) 1000, (a-4) 1100, (a-5) 1200, (a-6) 1400, (a-7) 1500, (a-8) 1600, (a-9) 1700, and (a-10) 1800 kFCI observed by using an MFM tip without protection layer before exposure to an environment of 70 °C and nearly 100% relative humidity. (b) Signal profiles along the white dotted lines in (a). (c) Power spectra analyzed for the magnetic bit images of (a).

$= [(\text{area}) / \pi]^{1/2}$. With increasing the exposure period from 0 to 10 days, the R_a value of magnetic film without protection layer increases from 0.6 to 1.8 nm. On the contrary, the R_a values of films with C, Si-N, and Si-C protection layers are kept constant around 0.5 nm during the oxidation test period. Furthermore, the average island radiuses of films with protection layers are smaller than those of films without protection layers. The results show that the film surface morphology is kept unchanged for the samples with protection layers, whereas the surface roughness changes with time for those without protection layers possibly depending on

the progress of iron material oxidation. As surface oxidation proceeds, Fe changes to oxides, FeO, Fe_2O_3, etc. which is related with the variations of crystal structure and density. The surface oxidation is enhancing the surface roughness estimated as R_a and island radius shown in Fig. 1.

Figures 2(a) and (c) show the SEM images observed for Si tips of 4 nm radius. Figures 2(b-1) and (b-2) show the SEM images observed for MFM tips without protection layers before and after exposure for 10 days, respectively. The Fe film thickness covering the base Si

Fig. 5 (a) MFM images of a perpendicular medium recorded at (a-1) 500, (a-2) 750, (a-3) 1000, (a-4) 1100, and (a-5) 1200 kFCI observed by using an MFM tip with C protection layer before exposure to an environment of 70 °C and nearly 100% relative humidity. (b) Signal profiles along the white dotted lines in (a). (c) Power spectra analyzed for the magnetic bit images of (a).

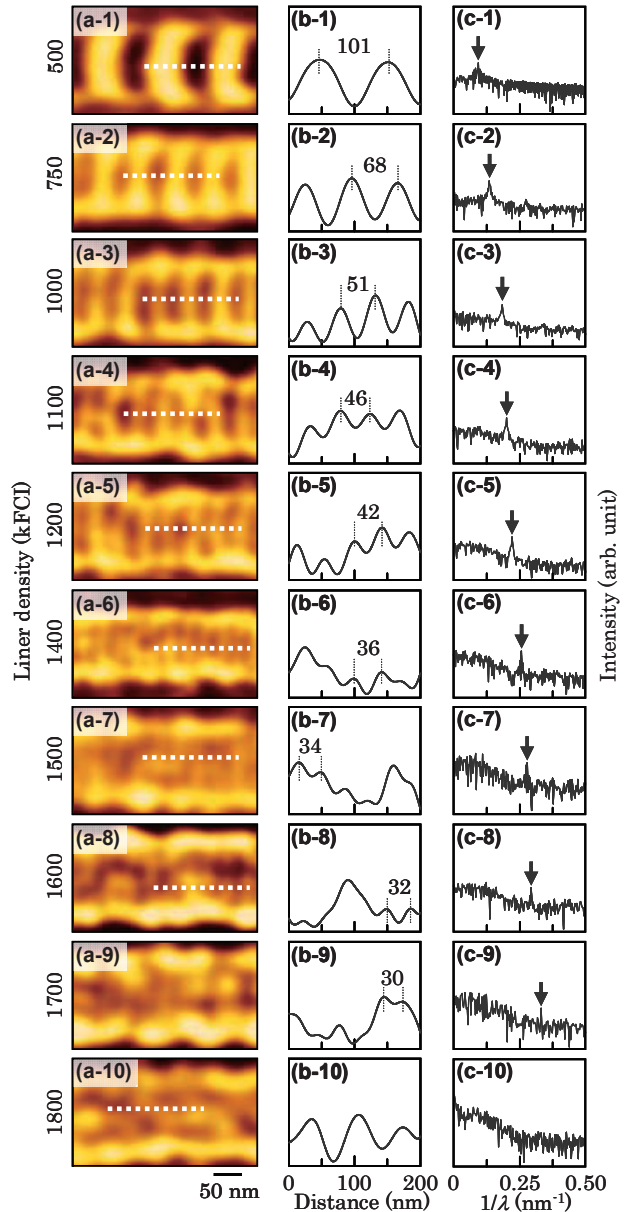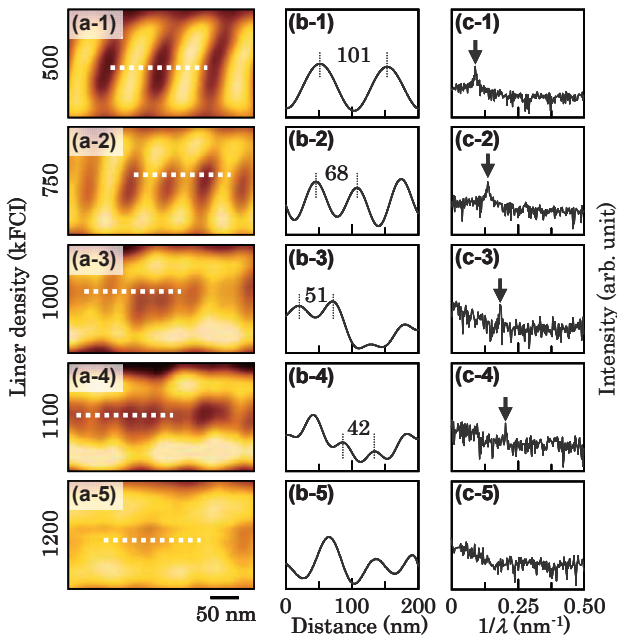**Fig. 6** (a) MFM images of a perpendicular medium recorded at (a-1) 500, (a-2) 750, (a-3) 1000, (a-4) 1100, (a-5) 1200, and (a-6) 1300 kFCI observed by using an MFM tip with Si-N protection layer before exposure to an environment of 70 °C and nearly 100% relative humidity. (b) Signal profiles along the white dotted lines in (a). (c) Power spectra analyzed for the magnetic bit images of (a).

Fig. 7 (a) MFM images of a perpendicular medium recorded at (a-1) 500, (a-2) 750, (a-3) 1000, (a-4) 1100, (a-5) 1200, and (a-6) 1300 kFCI observed by using an MFM tip with Si-C protection layer before exposure to an environment of 70 °C and nearly 100% relative humidity. (b) Signal profiles along the white dotted lines in (a). (c) Power spectra analyzed for the magnetic bit images of (a).
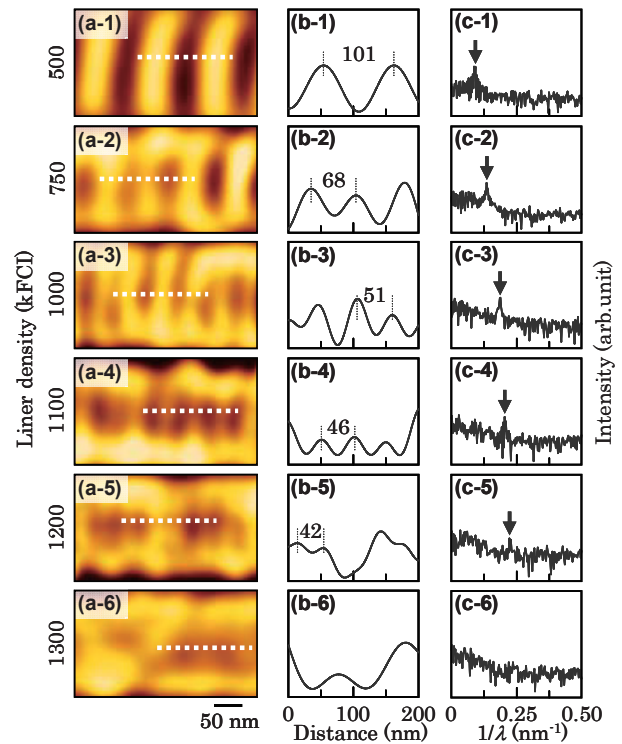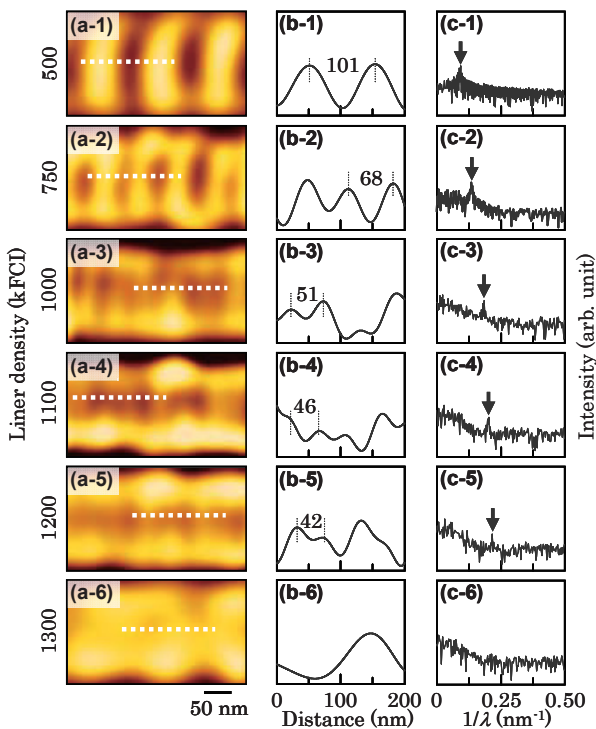
tip can be estimated by comparing the tip profile before and after Fe deposition. The thickness around the top part of MFM tip is measured to be about 12 nm which is 60% of thickness measured for a flat sample (20 nm). However, the film thickness is expected to vary delicately depending on the incidence angle of material sputtered-out from the target. The relatively large thickness ratio of about 60% with respect to that measured for the flat sample is due to a large size (3-inch diameter) of sputter target, the small size of Si tip, and the target to sample distance (150 mm). The local thickness of top part, which gives a dominant influence on the MFM performance, is considered to be similar to that measured for the flat sample, since the incident angle is almost same between the two cases. Therefore, the thickness measured for flat sample is employed as the effective coating thickness of MFM tip. As the exposure period increases from 0 to 10 days, the tip radius increases from 29 to 32 nm, corresponding to the film surface morphology variation observed for the flat film samples. Furthermore, the tip surface profile is changing to be very smooth losing the small surface undulations which are observed for the tip before exposure. Such variation is interpreted to be caused by the surface oxidation of coated Fe film. Figures 2(d-1) and (d-2) show the SEM images observed for MFM tips with C protection layers before and after exposure for 10 days, respectively. The thickness of C protection layer on the side of Si tip is estimated to be about 1 nm. The radius and the surface roughness are almost similar between the two samples, indicating that the magnetic tip structure is maintained even after
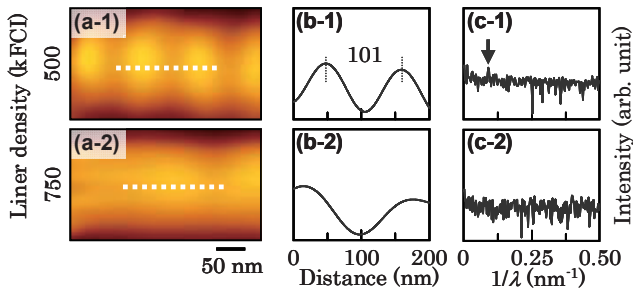
Fig. 8 (a) MFM images of a perpendicular medium recorded at (a-1) 500 and (a-2) 750 kFCI observed by using an MFM tip without protection layer after exposure to an environment of 70 °C and nearly 100% relative humidity for 10 days. (b) Signal profiles along the white dotted lines in (a). (c) Power spectra analyzed for the magnetic bit images of (a).

Fig. 9 (a) MFM images of a perpendicular medium recorded at (a-1) 500, (a-2) 750, (a-3) 1000, and (a-4)1100 kFCI observed by using an MFM tip with C protection layer after exposure to an environment of 70 °C and nearly 100% relative humidity for 10 days. (b) Signal profiles along the white dotted lines in (a). (c) Power spectra analyzed for the magnetic bit images of (a).

Fig. 10 (a) MFM images of a perpendicular medium recorded at (a-1) 500, (a-2) 750, (a-3) 1000, and (a-4) 1100 kFCI observed by using an MFM tip with Si-N protection layer after exposure to an environment of 70 °C and nearly 100% relative humidity for 10 days. (b) Signal profiles along the white dotted lines in (a). (c) Power spectra analyzed for the magnetic bit images of (a).

Fig. 11 (a) MFM images of a perpendicular medium recorded at (a-1) 500, (a-2) 750, and (a-3) 1000 kFCI observed by using an MFM tip with Si-C protection layer after exposure to an environment of 70 °C and nearly 100% relative humidity for 10 days. (b) Signal profiles along the white dotted lines in (a). (c) Power spectra analyzed for the magnetic bit images of (a).
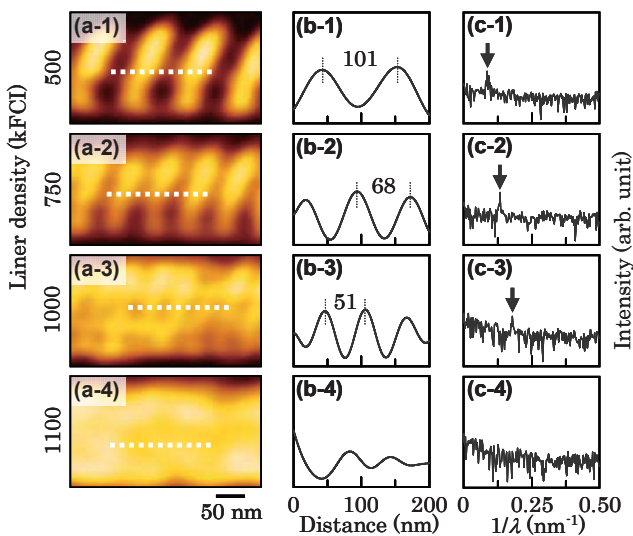
exposure to the environment of high temperature of 70 °C and high humidity of nearly 100% for 10 days. The results indicate that the protection layer coating is effective in keeping the tip profile by preventing surface oxidation of magnetic material. Figure 3 shows the variations of M_s measured for flat film samples with and without protection layers. The M_s values are almost similar to that of bulk bcc-Fe material (1713 emu/cm^3) for the samples with and without protection layers soon after preparation. The M_s value of film without protection layer decreases to 1150 emu/cm^3 after exposure for 10 days, whereas those of films with C, Si-N, and Si-C protection layers show small variations to 1700–1600, 1700–1500, 1700–1400 emu/cm^3, respectively. These results are suggesting that a high detection sensitivity is kept for a long time by introducing a thin protection layer on a magnetic tip.

Figure 4(a) shows the MFM images of a perpendicular medium recorded at linear densities ranging from 500 to 1800 kFCI observed by using an MFM tip without protection layer before oxidation. The sharpness of MFM image is degrading with increasing the linear density. In order to estimate the degradation quantitatively, MFM signal intensity profile measurement and fast Fourier transformation (FFT) analysis are carried out for the magnetic bit images of Fig. 4(a). Figures 4(b) and (c) show the intensity variation profiles measured along the white dotted lines in Fig. 4(a) and power spectra analyzed for the magnetic bits of Fig. 4(a), respectively. The bit lengths and the peaks corresponding to the recording

Fig. 12 Dependence of resolution on exposure period measured for MFM tips without and with C, Si-N, and Si-C protection layers.

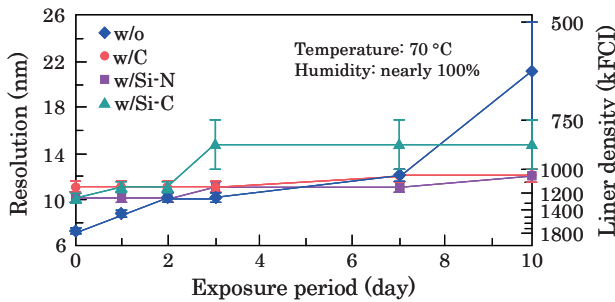densities ranging between 500 and 1700 kFCI are respectively recognized as shown in Figs. 4(b-1)–(b-9) and (c-1)–(c-9). Magnetic bits recorded at 1800 kFCI are not distinguishable as shown in Figs. 4(b-10) and (c-10). Therefore, the spatial resolution is between 14.9/2 = 7.5 nm (1700 kFCI) and 14.1/2 = 7.1 nm (1800 kFCI), that is, 7.3 ± 0.2 nm.

Figures 5, 6, and 7, respectively, show the MFM data obtained by employing tips with C, Si-N, and Si-C protection layers before exposure. When the tip with C protection layer is employed, the magnetic bits recorded below 1100 kFCI are observed, whereas those recorded at 1200 kFCI are not detected. The resolution is thus between 23.1/2 = 11.5 nm (1100 kFCI) and 21.2/2 = 10.6 nm (1200 kFCI), that is, 11.1 ± 0.4 nm. Similarly, the resolution is determined to be between 21.2/2 = 10.6 nm (1200 kFCI) and 19.5/2 = 9.8 nm (1300 kFCI), that is, 10.2 ± 0.4 nm for MFM tips with both Si-N and Si-C layers. The resolution slightly deteriorates by employing a protection layer. The total coating thickness is about 2 nm thinner for the tip without protection layer than that of a tip with protection layer. Therefore, the deterioration of resolution is considered mainly due to the increase of effective magnetic spacing between the top of magnetic tip and sample.

Figures 8–11 show the MFM data obtained by using MFM tips after exposure to the environment of 70 °C and nearly 100% humidity for 10 days. Figure 12 summarizes the variations of tip resolution as a function of exposure period. For tips without protection layer, the resolution apparently deteriorates with increasing the exposure period. The reason is partially due to an increase of tip radius because of Fe oxidation and partially due to a decrease in the MFM detection sensitivity. The date shown in Fig. 1(e), Fig. 3, and Fig. 12 are apparently supporting this interpretation. On the other hand, the resolutions of tips with C, Si-N, and Si-C layers are respectively almost constant at 12.1 ± 0.6 nm, 12.1 ± 0.6 nm, and 14.8 ± 2.1 nm. The result indicates that the introduction of C, Si-N, or Si-C protection layer is effective in keeping a high spatial resolution for a long period of time.

4. Conclusion

MFM tips are prepared by coating Fe films without and with C, Si-N, and Si-C protection layers on Si tips

and they are exposed to an environment of 70 °C and nearly 100% relative humidity, which is an acceleration test of about 10 times of room temperature environment (20 °C, 50%) . The resolution of MFM tip without protection layer deteriorates from 7.2 ± 0.2 nm to 21.2 ± 4.3 nm with increasing the exposure period from 0 to 10 days, whereas those with C, Si-N, and Si-C protection layers stay almost constant at 12.1 ± 0.6, 12.1 ± 0.6, and 14.8 ± 2.1 nm for 10 days. The protection layers are shown effective in preventing oxidation of Fe-coated MFM tips and thus contribute in keeping high spatial resolutions for a long period of time.

References

1) Z. Liu, Y. Dan, Q. Jinjun, and Y. Wu: *J. Appl. Phys.*, **91**, 8843 (2002).
2) G. N. Phillips, M. Siekman, L. Abelmann, and J. C. Lodder: *Appl. Phys. Lett.*, **81**, 865 (2002).
3) D. Litvinov and S. Khizroev: *Appl. Phys. Lett.*, **81**, 1878 (2002).
4) L. Gao, L. P. Yue, T. Yokota, R. Skomski, H. Liou, H. Takahashi, H. Saito, and S. Ishio: *IEEE Trans. Magn.*, **40**, 2194 (2004).
5) I. Utke, P. Hoffmann, R. Berger, and L. Scandella: *Appl. Phys. Lett.*, **80**, 4792 (2002).
6) H. Kuramochi, H. Akinaga, Y. Semba, M. Kijima, T. Uzumaki, M. Yasutake, A. Tanaka, and H. Yokoyama: *Jpn. J. Appl. Phys.*, **44**, 2077 (2005).
7) M. Rührig, S. Porthun, and J. C. Lodder: *J. Appl. Phys.*, **79**, 2913 (1996).
8) Z. Deng, E. Yenilmez, J. Leu, J. E. W. J. Straver, H. Dai, and K. A. Moler: *Appl. Phys. Lett.*, **85**, 6263 (2004).
9) K. Nagano, K. Tobari, K. Soneta, M. Ohtake, and M. Futamoto: *J. Magn. Soc. Jpn.*, **36**, 109 (2012).
10) M. Ohtake, K. Soneta, and M. Futamoto: *J. Appl. Phys.*, **111**, 07E339 (2012).
11) T. Hagami, K. Soneta, M. Ohtake, and M. Futamoto: *EPJ Web Conf.*, **40**, 01002 (2013).
12) S. Ishihara, T. Hagami, K. Soneta, M. Ohtake, and M. Futamoto: *J. Magn. Soc. Jpn.*, **37**, 56 (2013).
13) K. Soneta, M. Ohtake, and M. Futamoto: *J. Magn. Soc. Jpn.*, **37**, 107 (2013).
14) S. Ishihara, M. Ohtake, and M. Futamoto: *J. Magn. Soc. Jpn.*, **37**, 255 (2013).
15) M. Futamoto, T. Hagami, S. Ishihara, K. Soneta, and M. Ohtake: *IEEE Trans. Magn.*, **49**, 2748 (2013).
16) S. Saito, M. Futamoto, Y. Honda, T. Nishimura, and K. Yoshida: *IEEE Trans. Magn.*, **23**, 2398 (1987).
17) A. P. Grosvenor, B. A. Kobe, and N. S. Mclntyre: *Surf Sci.*, **574**, 317 (2005).

<Paper>

Development of First-Order Gradiometer-type MI Sensor and its Application for a Metallic Contaminant Detection System

T. Takiya, T. Uchiyama, and H. Aoyama*

Graduate School of Engineering, Nagoya Univ., *Chikusa-ku, Nagoya, Aichi 464-8603, Japan*
*Aichi Steel Co., *1 Wano-Wari, Arao-machi, Tokai, Aichi 476-8666, Japan*

A first-order gradiometer-type MI sensor that can reduce environmental magnetic noise without a magnetic shield was developed. The noise spectral density of this sensor is 20 pT/Hz$^{1/2}$ at 1–30 Hz, which is as good as a commercial fluxgate sensor, and the noise at 60 Hz relating to the power source line is reduced. We detected SUS304 austenitic stainless steel balls with the developed MI gradiometer to simulate a system for detecting metallic contaminants using the MI sensor. The variation of magnetic field with moving SUS304 balls corresponds to the theoretical value obtained for the model of a steel ball. This MI sensor without a magnetic shield system provides a compact and simple method of detecting metallic contaminants.

Key words: MI sensor, gradiometer, fluxgate magnetometer, metallic contaminant detection system

1. Introduction

High-sensitivity magnetometers are used in industry, for measurement of biomagnetism, and other applications. The magneto-impedance (MI) sensor can detect microscopic magnetic signals ranging from mT (10^{-3} T) to pT (10^{-12} T) by utilizing the magneto-impedance (MI) effect [1]. In the MI effect, the impedance of an amorphous wire changes significantly when a high-frequency current is passed through the amorphous wire [2]. A CMOS-MI sensor which can discriminate magnetic poles by measuring the voltage induced in a pick-up coil wound with amorphous wire was developed in 2002 [3].

MI sensors have been studied for use in various fields [4]–[6]; we are considering utilizing the MI sensor for non-destructive inspections. Recently, there have been various cases of contamination of food, and metal accounts for 14% of all such contamination according to a national survey in 2014 [7]. Metal detectors or X-ray examination are the most common methods of detecting foreign metal substances. As a more sensitive detection method, a Superconducting Quantum Interference Element (SQUID) sensing system, which can detect the magnetic field relating to the residual magnetization of metal, has been developed [8]. The MI sensor also can detect metal substances using the measurement principle of SQUID, and a contaminant detection system with an MI sensor has been realized [9]. The advantage of the MI sensing method is that it can detect metal without a magnetic shield system by using a gradiometer comprising a pair of MI sensors. The MI sensor is expected to provide a compact, low-price system for detecting metallic contaminants in food.

In this study, we developed a first-order gradiometer-type MI sensor (MI gradiometer) that can reduce the influence of external magnetic noise, and measured the variation of magnetic field with moving SUS304 balls to simulate a metallic contaminant
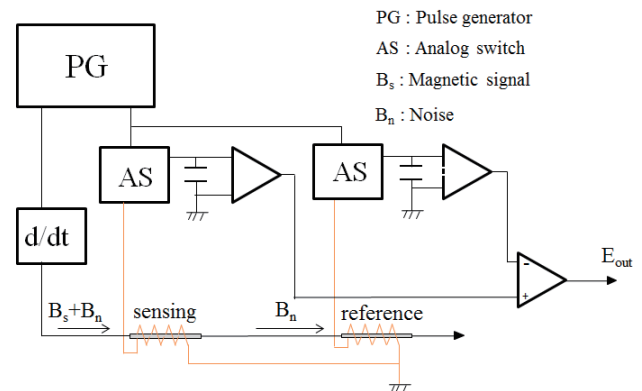
Fig. 1   First-order gradiometer type MI sensor.
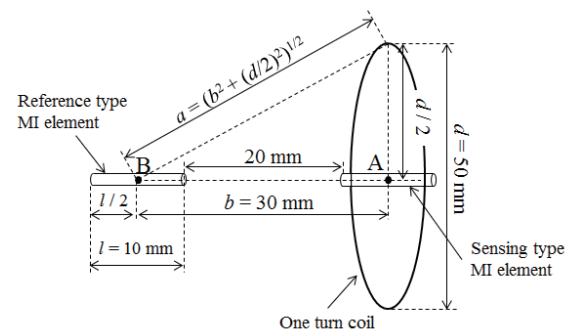
Fig. 2   Position of one-turn coil and MI elements.

detection system using the MI sensor.

2. First-order gradiometer-type MI sensor

The first-order gradiometer-type MI sensor (MI gradiometer) is composed of a pair of CMOS-MI sensors (Fig. 1). The high-frequency current is passed through a sensing-type and a reference-type MI element after the voltage is differentiated by a pulse generator (CMOS multi-vibrator). The MI gradiometer outputs the difference of the voltage induced in two pick-up coils: a wound sensing-type MI element and a reference-type MI

Fig. 3 Output of MI gradiometer when a sine voltage is applied to a one-turn coil.

Fig. 4 Comparison of external magnetic noise spectral density between MI gradiometer and fluxgate sensor.

element.

The length of the sensor head is 50 mm. The amorphous wire (Aichi Steel Co., Ltd.) used in the sensor head is 25 μm in diameter and 40 mm in length. The distance between the sensing and reference element is set at 20 mm from the center of both elements. The pick-up coils of each MI element have 700 turns. The frequency band of the MI gradiometer is 1–30 Hz. The magnetic sensitivity of the sensing MI element is $46×10^6$ V/T in a static magnetic field because the sensitivity is increased 1167 times with amplifiers. The magnetic sensitivity of t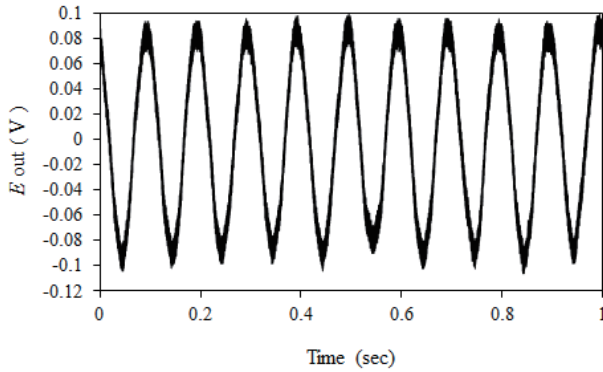he gradiometer is $1.53×10^9$ V/(T/m) when the magnetic sensitivity of the sensing element is divided by the distance (30 mm) between the sensing-type and reference-type MI elements.

We confirmed the operation of the developed MI gradiometer by detecting an artificial signal produced by a one-turn coil (diameter d = 50 mm, impedance z = 20 kΩ). Figure 2 shows a one-turn coil to which is applied sine voltage v (amplitude: 2 V, frequency: 10 Hz) set in the center of the sensing-type MI element (point A). According to Biot-Savart's law, Eq. (1) and (2) represent the magnetic flux density at point A, B_A, and point B, B_B.

$$B_A = \mu_0 H_A = \mu_0 (i / d) \tag{1}$$

$$B_B = \mu_0 H_B = \mu_0 [i (d / 2)^2 / 2b^3] \tag{2}$$

where H_A is the magnetic field at point A, H_B is the magnetic field at point B, i = v/z, d = 50 mm, b = $(b^2 + (d/2)^2)^{1/2}$, c = 30 mm, l = 10 mm, and μ_0 = $4\pi×10^{-7}$. Consequently, B_A is 2.51 nT and B_B is 0.662 nT.

The output of the MI gradiometer, E_{out}, is shown in Fig. 3. The average amplitude of E_{out} is 0.09 V and its frequency is 10 Hz. The detected magnetic signal of the MI gradiometer corresponds to 1.96 nT when E_{out} is divided by the magnetic sensitivity of the sensing-type MI element, $46×10^6$ V/T. This measured value approximates $B_A - B_B$ = 1.85 nT of the theoretical magnetic signal of the MI gradiometer. Therefore, the developed MI gradiometer operates correctly.
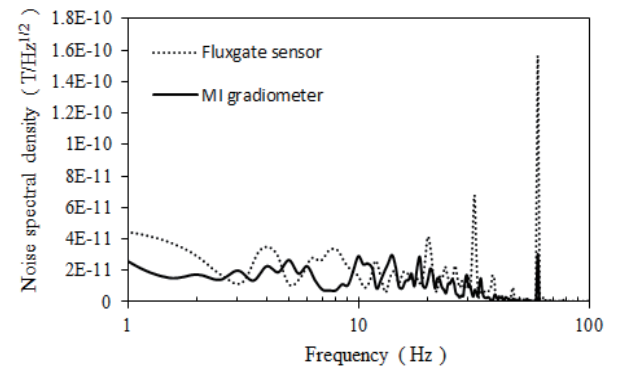
3. Comparison with a fluxgate sensor

We measured the environmental magnetic noise spectral density in the laboratory with the MI gradiometer and a fluxgate sensor (Fluxmaster, Stefan Mayer Instruments). The magnetic sensitivity is $46×10^6$ V/T for the sensing-type MI element of the MI gradiometer and 10 V/μT for the fluxgate sensor in a static magnetic field, and both sensors are set to a cut-off frequency of 30 Hz with a multi-function filter (3611, NF Corporation).

The environmental noise spectral density is shown in Fig. 4. The magnetic noise at 1 Hz is 40 pT/Hz$^{1/2}$ in the fluxgate magnetometer and 20 pT/Hz$^{1/2}$ in the MI gradiometer. The noise at 60 Hz relating to the power source line reaches about 160 pT/Hz$^{1/2}$ in the fluxgate sensor, whereas that of the MI gradiometer is 30 pT/Hz$^{1/2}$ and the noise at 30 Hz also is reduced significantly. This result indicates that the MI gradiometer is robust against environmental magnetic noise.

4. Detection of SUS304 balls using MI sensor

Firstly, we detected SUS304 austenitic stainless steel balls with the MI gradiometer. Figure 5 is a photograph of a SUS304 ball which was used for the experiment and Table 1 lists the chemical composition of SUS304 according to the JIS standard. SUS304 is a corrosion-resistant stainless steel widely used in products ranging from household items to industrial goods. SUS304 is nonmagnetic austenite (face-centered-cubic structure) but when stress is applied the metal becomes magnetized due to the formation of martensite [10]. Figure 6 shows the set-up for measuring the variation of magnetic field when the SUS304 ball was moved at various distances, r, from the sensor head to the steel ball. The SUS304 ball was placed on a turntable rotated at 7.5 m/min. The diameter of the SUS304 ball, d_S, was 0.15 mm, 0.3 mm, 0.5 mm, 0.8 mm, 1.0 mm and 1.5 mm.
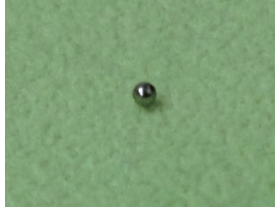
Fig. 5   Stainless steel ball of SUS304 (1.0 mm diameter).

Table 1   Chemical composition of SUS304

Element	C	Si	Mn	P	S	Ni	Cr
Mass%	$\leqq$ 0.08	$\leqq$ 1.00	$\leqq$ 2.00	$\leqq$ 0.045	$\leqq$ 0.030	8.00 ~ 10.50	18.00 ~ 20.00

We compared the theoretical value of magnetic field of the model of the steel ball (Fig. 7) and the value measured with the MI gradiometer, ΔB. The external magnetic field of the SUS304 ball, H, at point p is given by Eq. (3) which is obtained from Fig. 7 [11].

$$B = \mu_0 H = \mu_0 (m / 2 \pi \mu_0 r^3) \cos\theta \qquad (3)$$

Where $ds \ll r$, B is the magnetic flux density and m is the residual magnetic moment of SUS304. θ is assumed to be 0° since SUS304 is magnetized in the longitudinal direction of an amorphous wire by using a permanent magnet. We measured m with a VSM. The residual magnetic field of the VSM was calibrated with a gauss meter and we postulated that m is the residual magnetic moment when the magnetic field of electromagnets is 0.
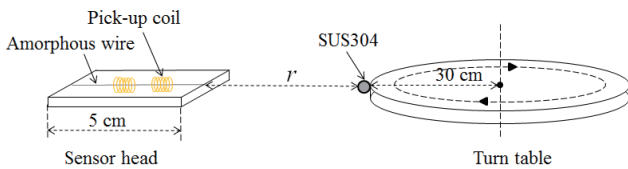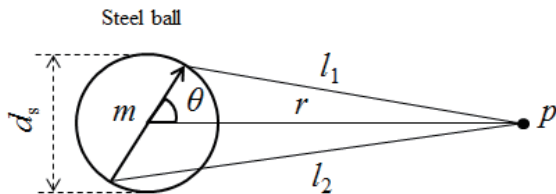

Fig. 6   Measurement setup for SUS304.

Fig. 7   Model of steel ball.

Figure 8 shows the output voltage of the MI gradiometer, E_{out}, for the moving SUS304 ball of each diameter when r was 10 mm. The maximum E_{out} is 3.0 V at ds = 1.5 mm, and the minimum is 90 mV at ds = 0.15 mm. However, E_{out} is not proportional to ds but is proportional to m. We consider that this phenomenon results from the difference in processing degree of each
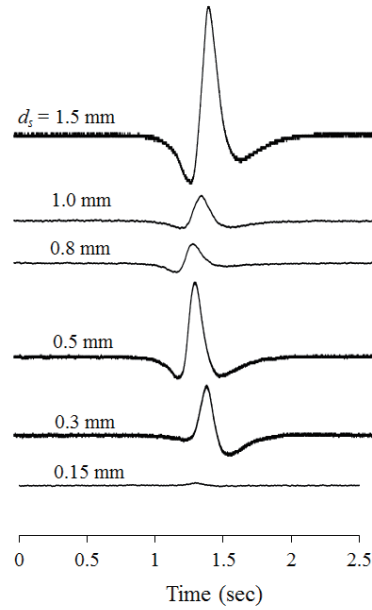
Fig. 8   Output voltage of MI gradiometer with movement of SUS304 steel balls.
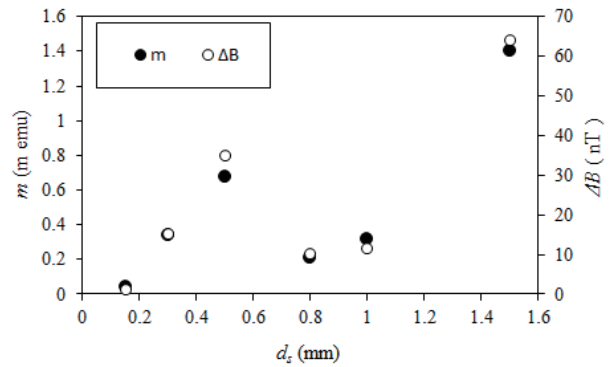
Fig. 9   Relationship between residual magnetic moment, m, and value measured with MI gradiometer, ΔB.

SUS304 ball. ΔB is calculated by dividing E_{out} by 46×10^6 V/T and Fig. 9 confirms that ΔB is proportional to m.

Secondly, we examined the lowest limit of AC magnetic field of the MI gradiometer without a shield box made of permalloy. We estimate that the detection for SUS304 ball of 0.3 mm diameter is the benchmark of performance evaluation because the lowest detection limit of the X-ray detector is about 0.6–0.7 mm diameter[12]. For this reason, the detection target of the MI gradiometer is an SUS304 ball of ds = 0.3 mm. In addition, we detected a SUS304 ball with the fluxgate sensor "Fluxmaster". Since the maximum rotational velocity of the turntable which we used is 7.5 m/min, the cut-off frequency of both sensors was set at 30 Hz with the 3611 multi-function filter.

Figure 10 shows the dependence of the variation of the magnetic field with moving SUS304 ball and various distances between sensor head and SUS304 ball. Figure 10(a) compares ΔB between the measured value and the theoretical value derived from Eq. (3). The measured

Table 2 Comparison between existing contaminant detection system and MI sensor system.

|	Detection lowest limit	Unusable food	Detection without metal
Metal detector	Depends on conductivity of metal substance	No food	×
X-ray	ϕ 0.6–0.7 mm	Dairy products	○
MI sensor	ϕ 0.3 mm	No food	×

value is calculated by dividing E_{out} by the magnetic sensitivity of the sensing-type MI element (46×10^6 V/T). For example, when r was fixed at 5 mm, the theoretical value of B was calculated from Eq. (3) for each distance r from 5 mm to 14 mm because the length of a sensing-type MI element is 10 mm. The average B value was then calculated. Similarly, we calculated the average B value of a reference-type MI element. The theoretical value of ΔB was taken as the difference between the average B values of the sensing and reference-type MI elements. The measured value of ΔB corresponds with the theoretical value and the lowest ΔB is 1.20 nT at $r = 30$ mm in Fig. 10(a). Figure 10(b) shows the measurement result when using the fluxgate sensor. The lowest magnetic flux density is 5.28 nT at $r = 20$ mm. Figure 11 shows the output of both sensors at $r = 25$ mm. The MI gradiometer reduces the environmental magnetic noise compared with the fluxgate sensor and the detected signal is clear.

We considered a system for detecting contaminants using the MI gradiometer. We estimate that the smallest stainless steel ball with weak magnetism like SUS304 that can be detected is 0.3 mm in diameter assuming that several MI gradiometers are located at the top and bottom of the belt conveyor. For example, frozen food packages can pass between MI sensors in this case. Metal detectors and X-ray examination are the most common methods used for contaminant detection. Table 2 compares the general method and the MI sensor system. The sensitivity of a metal detector depends on the conductivity of a metal contaminant. Magnetic metallic contaminants can be easily detected by magnetizing them. X-ray examination can detect a broad range of foreign substances such as stone, glass, bone, resin as well as metal, but cannot be used for dairy products because of the ionization of food or the extinction of good bacteria by the X-rays. To overcome these problems, the SQUID sensing method has a sensitivity higher than pT (10^{-12} T) and some SQUID detection systems for detecting contaminants in food have been developed [13]–[16]. The maximum velocity of the belt conveyor of a SQUID detection system is about 100 m/min [8], but the contaminant detection system using the MI gradiometer is at the design stage and SUS304 balls are moved at 7.5 m/min to correctly measure the magnetic signal of the stainless steel balls. On the other hand, the installation and maintenance costs are higher as SQUID needs a cooling device with liquid helium and
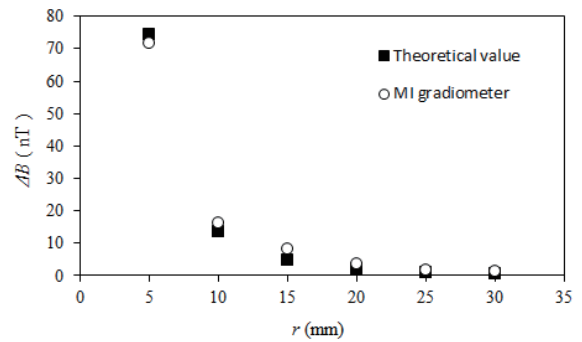
(a) Comparison between value measured with MI gradiometer, ΔB, and theoretical value derived from Eq. (3)
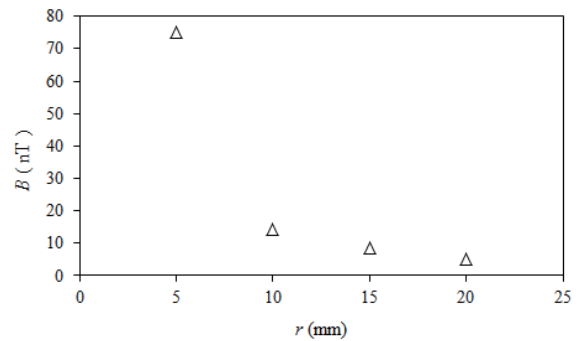
(b) Value measured with fluxgate sensor

Fig. 10 Dependence of variation of magnetic field with movement of SUS304 ball (0.3 mm diameter) and various distances r between sensor head and steel ball.
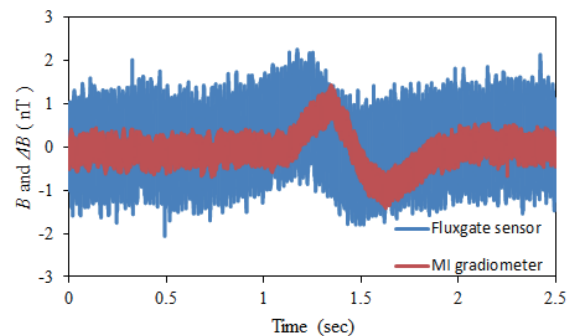

Fig. 11 Comparison between output of MI gradiometer and fluxgate sensor at $r = 25$mm.

magnetic shield system. Since the MI gradiometer can reduce the environmental magnetic noise without the magnetic shield, we consider that the MI sensor is a compact, simple method that can detect small metallic contaminants.

5. Conclusions

We developed a first-order gradiometer-type MI sensor (MI gradiometer) and used it to detect SUS304 stainless steel balls.

First, we confirmed that the developed MI gradiometer operated correctly by measuring an artificial signal (amplitude: 2.5 nT, frequency: 10 Hz) with a one-turn coil. The environmental magnetic noise of the MI gradiometer from 1 Hz to 30 Hz was about 20 $pT/Hz^{1/2}$. In particular, noise at 60 Hz relating to the power source line was reduced by at least 1/5 compared with a commercial fluxgate sensor.

Secondly, we measured the variation of the magnetic field with a moving SUS304 ball by using the MI gradiometer and fluxgate sensor. SUS304 balls were magnetized toward the sensor head and were rotated at 7.5 m/min on a turntable. The value measured with the MI gradiometer, ΔB, corresponded with the theoretical value calculated by Eq. (3). When we measured a SUS304 ball of 0.3 mm diameter, the lowest detectable magnetic field of each sensor was 1.20 nT (MI gradiometer) and 5.28 nT (Fluxgate sensor).

Since the developed MI gradiometer could detect the magnetic field of SUS304 balls of 0.15 mm, 0.3 mm, 0.5 mm, 0.8 mm, 1.0 mm and 1.5 mm diameters, we consider that the MI sensor can be used in a system for detecting metallic contaminants and that the risk of metal remaining in food can be reduced by using this sensor together with an existing system such as X-ray examination.

References

1) E. Portalier, B. Dufay, S. Saez, and C. P. Dolabdjian : *10th European Conference on Magnetic Sensors and Actuators* (EMSA14), (2014).
2) L. V. Panina and K. Mohri : *Appl. Phys. Lett.*, **65** (90), 1189–1191 (1994).
3) C. M. Cai, Y. Nakamura, K. Mohri, Y. Honkura, and M. Mori : *J. Magn. Soc. Jpn.*, **26** (4), 551–554 (2002).
4) S. Godoshnikov, N. Usov, A. Nozdrin, M. Ipatov, A. Zhukov, and V. Zhukova : *Status Solidi A*, DOI 10.1002/pssa.201300717, (2014).
5) B. Dufay, S. Saez, C. P. Dolabdjian, A. Yelon, and D. Menard: *IEEE Sensors Journal*, **13** (1), 379–388 (2013).
6) B. Dufay, S. Seaz, C. Dolabdjian, A. Yelon, and D. Menard: *EEE Transactions on Magnetics*, 49 (1), 85–88 (2013).
7) Incorporated Administrative Agency National Life Center news release document: "Consultation and summary about the alien substance mixture of the food" (2015).
8) S. Tanaka : *Journal of the Japanese Society for Non-Destructive Inspection*, **63** (11), 556–561 (2014).
9) T. Uchiyama : *Journal of the Japanese Society for Non-Destructive Inspection*, **63** (11), 562–566 (2014).
10) K. Miura, S. Kobayashi, Y. Kamada, Y. Onuki and J.A. Szpunar : *J. Japan Inst. Met. Mater*, **78** (10), 375–380 (2014).
11) K. Ota: "*Jikikugaku no Kiso*", 25–26 (Kyoritsuzensyo, Tokyo, 1973).
12) H. Watabiki, T. Takeda, S. Mitani, T. Yamazaki, M. Inoue, H. Koba, I. Miyazaki, N. Saito, S. Wada, T. Kanai : *Anritsu Technical*, No.87, 53–59 (2012).
13) T. Nagaishi, H. Ota, K. Nishi, K. Kuwa, T. Fujita, and S. Tanaka : *IEEE Trans. Appl. Supercond.*, **17** (2), 800–803 (2007).
14) S. Tanaka, H. Fujita, Y. Hatsukade, T. Nagaishi, K. Nishi, H. Ota, T. Otani, and S. Suzuki : *Supercond. Sci. Technol.*, **19**, S280-S283 (2006).
15) H. J. Krause, G. I. Panaitov, N. Wolter, D. Lomparski, W. Zander, Y. Zhang, E. Oberdoerffer, D. Wollersheim, and W. Wilke : *IEEE Trans. Appl. Supercond.*, **15** (2), 729–732 (2005).
16) M. Bick, P. Sullivan, D. L. Tilbrook, J. Du, B. Thorn, R. Binks, C. Sharman, K. E. Leslie, A. Hinsch, K. Macrae, and C. P. Foley : *Supercond. Sci. Technol.*, **18**, 346–351 (2005).

<Paper>

Detection and Distinction of Conductive and Magnetic Security Markers Using Eddy-Current Inspection

T. Minamitani, S.Yamada

Institute of Nature and Environmental Technology, Kanazawa University, *Kakuma-machi, 9201192, Japan*

A printed magnetic marker is used effectively on bills or check for security. In securing of valuable documents, a further improvement in the degree of security is always indispensable. The addition of a conductive marker as well as a magnetic marker enhances the value of information and the reliability of these markers. We applied an eddy-current testing (ECT) technique by using the micro ECT probe with a giant magneto-resistance element (GMR) to detect both markers. Two markers can be detected and also distinguished by recognizing both the amplitude and phase of the ECT signal. This paper describes the method of detection and the results for these markers printed by a magnetic and conductive ink.

Keywords：Eddy-current inspection, GMR sensor, security, conductive marker, magnetic marker, discrimination.

1. Introduction

The magnetic apparatus for security identification uses a semiconductor magnetic resistance element or a pick-up coil as a magnetic detector. The apparatus detects the magnetic-ink marker or magnetic thread security identifier on a bill or check, and recognizes the truth or falsehood of the identifier. The conductive ink that includes nano-particles was developed recently and is easy to print out on a paper medium using an ink-jet printer similar to that of a magnetic ink [1]. The simultaneous detection and identification of both markers will contribute to an increase in security.

The authors developed an inspection process for printed circuit board traces using an eddy-current testing (ECT) probe with a giant magneto-resistance element (GMR). It enables us to detect disconnections and chipping errors on a high-density printed circuit board [2]~[7]. The ECT probe consists of a meander exciting coil excited by a few MHz current and a GMR sensor that is a few μm in width. The defects on a printed trace with a hundred μm width could be inspected. The probe can detect the magnetic field distribution near magnetic trace with the same size.

The paper describes that the proposed ECT probe can detect and discriminate both magnetic and conductive markers. The detection principle depends on the construction and characteristics of the ECT probe with GMR sensor and exciting coil [2],[3]. The difference of the ECT signals between two markers is described using a numerical analysis and experimental results.

2. Measurement of Markers

2.1 Signal of magnetic and conductive markers by ECT

Figs. 1(a) and (b) show the principle and difference between detecting conductive and magnetic markers using ECT technique [8], [9]. Two kinds of markers are located vertically and are subjected to uniform AC exciting fields. In a conductive marker, eddy currents flow around the marker, and a penetrated magnetic flux can't penetrate into the marker. On the other hand, external magnetic fields are concentrated near a magnetic marker. When a scanned GMR sensor has sensitivity in the positive x-direction, the x-direction component B_x of magnetic fields near the point P1 has the difference distribution between conductive and magnetic markers as shown in Fig. 1. The phase of the detecting signal between the two markers becomes opposite in the presence of an AC exciting signal. When a GMR sensor is scanned across a marker, the phenomenon at the edge P1 also occurs at the edge P3 of the marker definitely and the phase is reversed. The x-component B_x of the magnetic fields disappears at the center P2 of the marker.
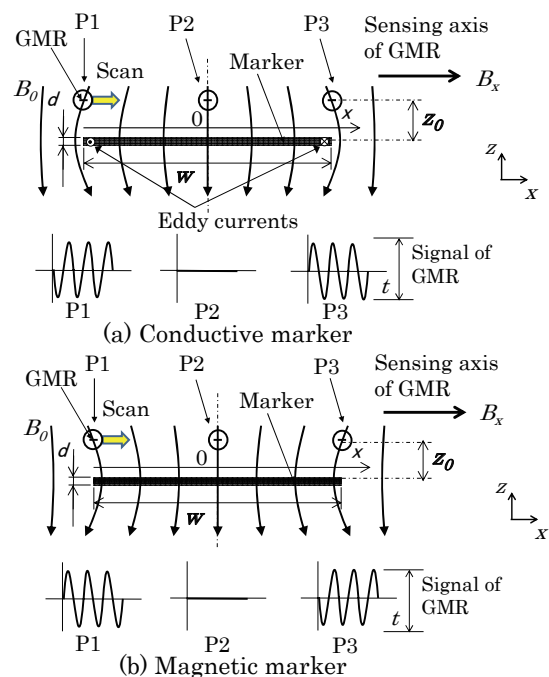

Fig. 1 Differences of AC magnetic fields near the edge of the markers.

It is assumed that the extension of the marker in the y-direction is long and a uniform external AC magnetic field $\mu_0 H_0$ ($= B_0$, z-component only) is applied to the marker in a vertical direction. A GMR sensor is installed to extract only the x component of the magnetic fields up only. The output voltage of a GMR with an angular frequency ω is,

$$V(x,t) \propto B_x(\mathrm{x}) \sin(\omega t + \phi), \qquad (1)$$

where $B_x(x)$ is the amplitude of the magnetic flux density at z_0 on a marker strip and ϕ is the phase shift with respect to the external applied fields.

For a magnetic marker (conductivity $\sigma = 0$), an external magnetic field is concentrated on a marker in Fig. 1(b) and the phase ϕ in Eq. (1) is given by

$$\phi = 0 \ (\mathrm{x} < 0), \qquad \phi = -\pi \ (\mathrm{x} > 0). \qquad (2)$$

For a conductive marker (permeability $\mu^* = 1$), the phase of the magnetic flux density affected by eddy currents is shifted depending on the conductivity and shape of a marker. We assume an equivalent eddy-current circuit with magneto-motive force, equivalent resistance R_e, and inductance L_e [10]. An equivalent eddy current $i_e(t)$ is,

$$i_e(t) \propto \{\omega B_0 / (R_e^2 + (\omega L_e)^2)^{1/2}\} \sin(\omega t + \pi/2 - \theta_0), \quad (3)$$

where

$$\tan \theta_0 = \omega L_e / R_e. \qquad (4)$$

For a conductive marker, magnetic fields near a marker are restrained by eddy currents and the x-component of the magnetic flux density is given by

$$\phi = -\pi \ (\mathrm{x} < 0), \qquad \phi = 0 \ (\mathrm{x} > 0). \qquad (5)$$

According to Eqs. (4) and (5), the output voltage is expressed as,

$$V(x,t) \propto B_x(\mathrm{x}) \sin(\omega t + \pi/2 - \theta_0 + \phi). \qquad (6)$$

If a conductive marker has low conductivity and the condition ($\omega L_e \ll R_e$) is satisfied, the phase θ_0 is 0. The phase of the output voltage is then shifted from $-\pi/2$ to $\pi/2$ at $x = 0$ when scanning the sensor in the x-direction. For the marker with high conductivity ($\omega L_e \gg R_e$), the phase is from $-\pi$ to 0. For a prescribed value of conductivity, the phase is considered to be the mean of the both values. The phase change experienced during an x-direction scan of the sensor is summarized in Table 1. The phase movements of the conductive and magnetic markers are reversed with respect to each other.

Fig. 2 shows the amplitudes of both markers including phase signal. When the pick-up sensor is close to the edge of the marker at the positions, P1 and P3, the signal becomes the maximum and minimum peak value respectively. The signal vanishes at the position P2. The output waveform of the magnetic marker has a reversed pattern compared to the conductive marker.

Table 1 Phase of sensor signal to external magnetic fields.

Material of marker	Condition	Position of sensor	
		x < 0	x > 0
Magnetic	$\mu^* > 1$, $R_e = \infty$	0	$-\pi$
Conductive	$\omega L_e \ll R_e$	$-\pi/2$	$\pi/2$
	$\omega L_e \gg R_e$	$-\pi$	0

2.2 Analysis of magnetic fields near markers

Fig. 2 shows the qualitative signal patterns for two kinds of markers. The waveform of magnetic fields depends on the exciting frequency, the material properties (conductivity and permeability), and the shape of the marker. The magnetic fields were calculated by using a 2D FEM. The simulated model and the sensing position are shown in Fig. 3. The marker was located under the uniform magnetic field with only a z-component ($B_0 = 1$ mT, $f = 5$ MHz). We simulated the amplitude of the x-component $B_x(x)$ and the phase with respect to the applied magnetic fields at $z_0 = 0.3$ mm on the surface of a marker.

We considered the marker models with different properties and a shape of $w = 2$, $d = 0.05$ mm. Fig. 4 shows the amplitude and phase of the magnetic flux density B_x. A solid line shows the amplitude of magnetic flux density, and a broken line is the phase with respect to the applied external fields at the edges, P1 and P3, of
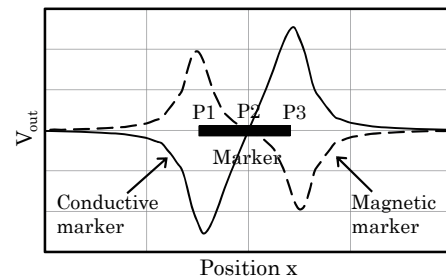
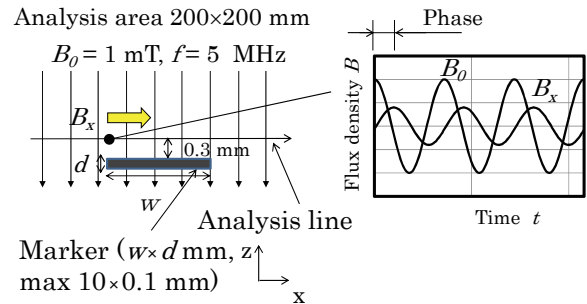**Fig. 2** Magnitude of B_x signal considering phase.

Fig. 3 Model of 2D FEM analysis.

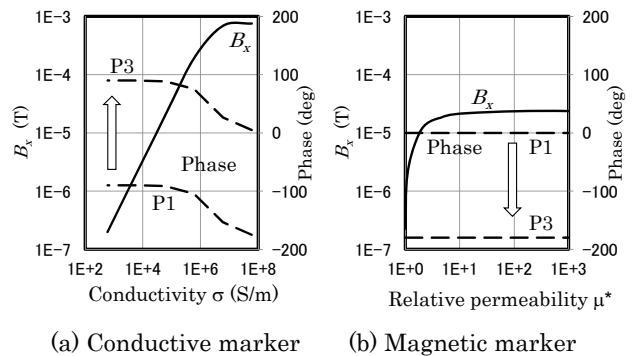(a) Conductive marker　　(b) Magnetic marker

Fig. 4 Amplitude and phase of magnetic flux density vs. conductivity and permeability.

the marker. The magnetic flux density increases with increasing conductivity of a conductive marker. The phase changes by keeping the phase difference of π between the positions, P1 and P2. A magnetic shielding effect by eddy currents at a high conductivity shifts the phase to π/2 with increasing conductivity. On the contrary, as permeability rises in the case of a magnetic marker, the magnetic flux density increases, and the phase is constant.

Fig. 5 shows the amplitude and phase of magnetic flux density for different materials. Figs. 5(a) and (c) show the simulation results for the markers printed using conductive and magnetic ink. For comparison, the result for a metallic marker (Cu) with high conductivity is shown in Fig. 5(b). These results show that the amplitude of magnetic flux density has a peak at both edges of a marker, and the order of amplitude from

highest to lowest becomes metal, a conductive ink, and magnetic ink marker. When a sensor passes by these markers, the change of phase signal is remarkably different between conductive and magnetic markers. The result suggests that the discrimination between both markers is possible because of the different behaviors of a phase.

Figs. 6 and 7 show the simulation results for amplitude and phase of magnetic flux density for three typical materials. When a marker shape becomes wide and thick, the magnetic flux density of all markers tends to increase. There is a little difference in the magnetic flux density as the thickness changes under the condition, $w >> d$.
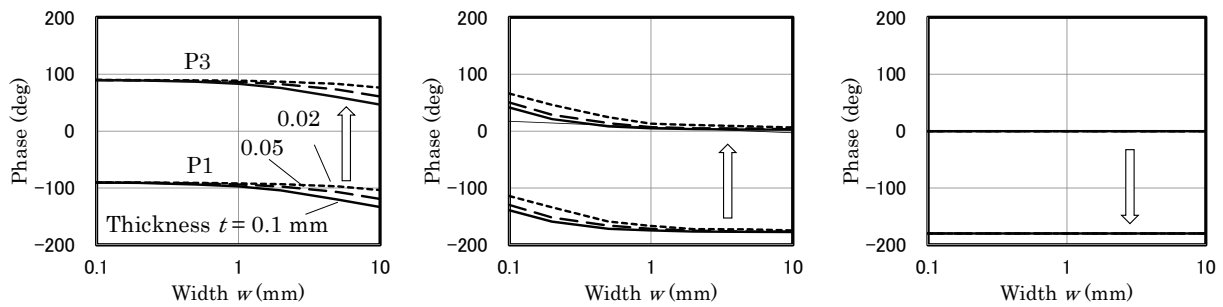
For a conductive-ink marker, the condition ($\omega L_e << R_e$) in Table 1 is satisfied, thus the phase is shifted from $-\pi/2$ to $\pi/2$ between the positions, P1 and P3. As the
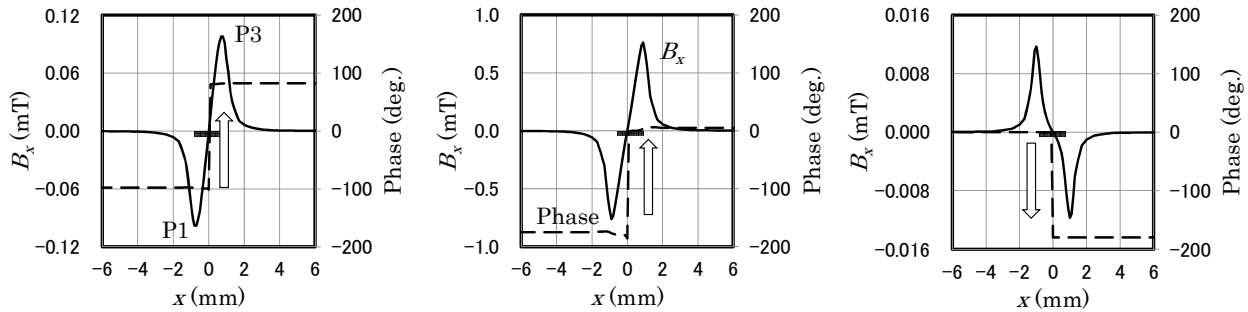
(a) Conductive ink ($\mu^* = 1$, $\sigma = 3 \times 10^5$ S/m) (b) Metal ($\mu^* = 1$, $\sigma = 6 \times 10^7$ S/m) (c) Magnetic ink ($\mu^* = 10$, $\sigma = 0$)

Fig. 5 Signal patterns of magnetic flux density for markers with different materials.
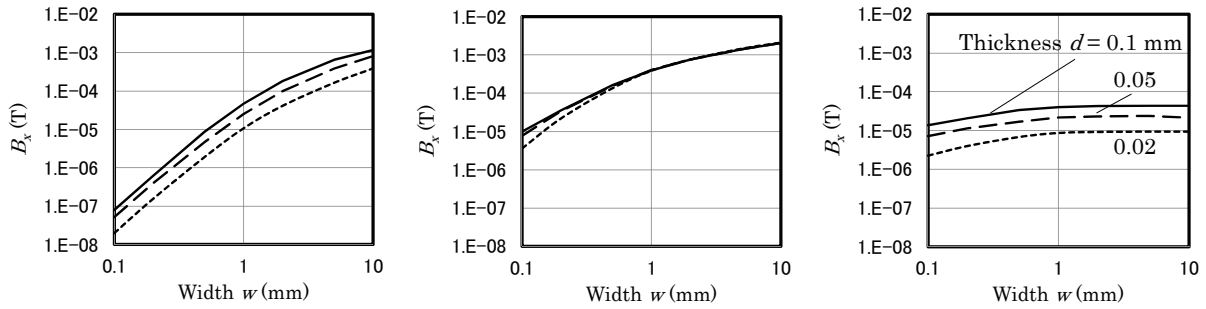
(a) Conductive ink ($\mu^* = 1$, $\sigma = 3 \times 10^5$ S/m) (b) Metal ($\mu^* = 1$, $\sigma = 6 \times 10^7$ S/m) (c) Magnetic ink ($\mu^* = 10$, $\sigma = 0$)

Fig. 6 Amplitude of magnetic flux density as a function of width and thickness of markers.

(a) Conductive ink ($\mu^* = 1$, $\sigma = 3 \times 10^5$ S/m) (b) Metal ($\mu^* = 1$, $\sigma = 6 \times 10^7$ S/m) (c) Magnetic ink ($\mu^* = 10$, $\sigma = 0$)

Fig. 7 Phase of magnetic flux density as a function of width and thickness of markers.

width increases, the phase characteristics change a little. On the contrary, the condition ($\omega L_e \gg R_e$) in Table 1 is satisfied for a metal marker with high conductivity.

According to these results, we concluded that two kinds of markers can be distinguished by recognizing both amplitude and phase of the ECT signal.

3. Experimental Measurement of Markers

3.1 Experimental apparatus

Fig. 8 shows the outline of the testing equipment with the ECT probe. The ECT probe has an exciting coil with a meander structure and dimensions of 0.2, 10, and 0.035 mm in width, length, and thickness respectively.
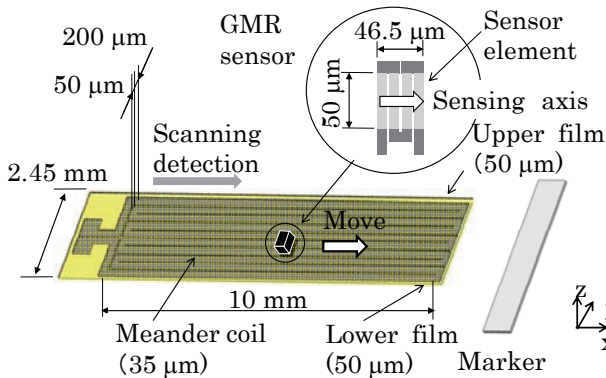

Fig. 8 Structure of ECT probe.

Fig. 9 Measurement system.

The pick-up element is giant magneto-resistance sensor with footprint 50×50 μm. The meander coil induces x-direction eddy currents along the trace of meander coil on a testing object. The GMR sensor detects the x-direction magnetic fields parallel to the induced eddy currents. When the probe is scanned orthogonal to a strip marker, the signal appears near both edges of the markers.

The block diagram of the measuring system for the ECT signal is shown in Fig. 9. There are three blocks, consisting of a high frequency generator and power amplifier for the exciting coil, xy-stage for scanning probe, and digital phase detector for the ECT signal. The reference signal of the phase detector is the exciting current. The amplitude and phase of the ECT signal are then detected.

3.2 Experimental results of different marker materials

Fig. 10 shows the amplitude of the ECT signals including phase for the following kinds of markers, conductive-ink, metallic, and magnetic-ink marker. The metallic marker is made of copper film. The conductivity of the conductive-ink marker depends on the printing condition. The value of conductivity for the printed conductive marker was 2×10^6 S/m experimentally derived by 4-point probe method and is about 3 % of the value for copper. The magnitude of the output voltage from lowest to highest for the given materials is in the following order metal, conductive ink, and magnetic ink. The pattern of the signal is similar to the simulated one shown in Fig. 5. We can recognize the definite difference of the pattern between conductive and magnetic markers from the experimental results.

Figs. 11 and 12 show the experimental results for amplitude and phase shift of the ECT signal on the markers with a 50 μm thickness and the widths from 1.0 to 10 mm. When the width of a marker becomes narrow, the output voltage of the signal tends to decrease. The phase shifts by about -π for a conductive marker and by +π for magnetic marker. These results confirm that the detection of a phase change enables us to distinguish between a magnetic-ink and conductive-ink marker. The possibility of distinguishing between two kinds of markers was confirmed also by experiments.

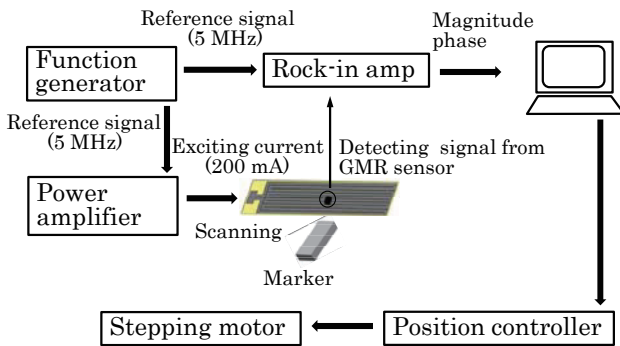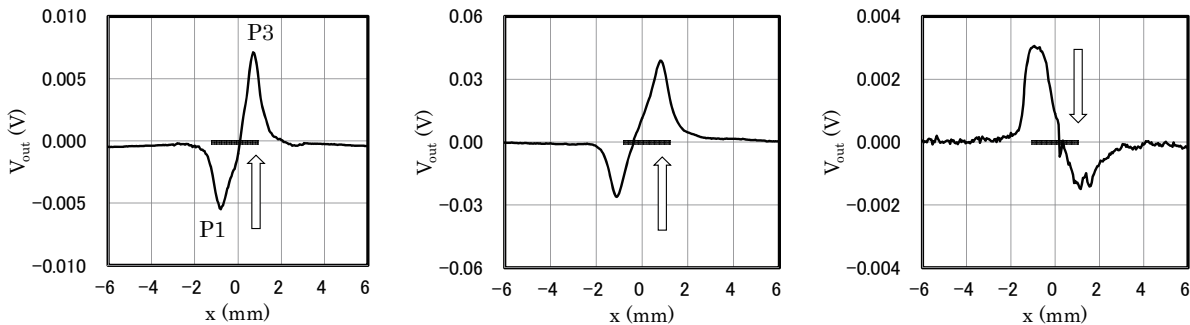(a) Conductive ink ($\mu^* = 1$, $\sigma = 2 \times 10^6$ S/m)　　(b) Metal ($\mu^* = 1$, $\sigma = 6 \times 10^7$ S/m)　　(c) Magnetic ink ($\mu^* = 1.05$, $\sigma = 0$)

Fig. 10 Signal patterns of ECT signals for markers with different materials.
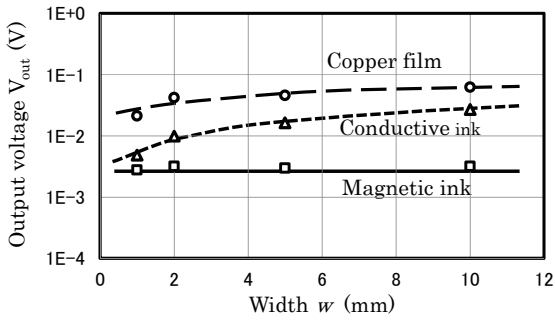
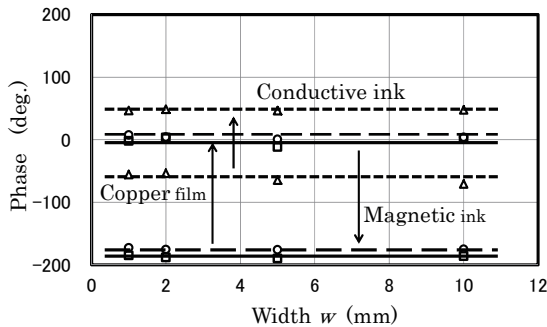**Fig. 11** Amplitudes of signal vs. width of markers with different materials.

Fig. 12 Phase shift vs. width of markers with different materials.

4. Conclusions

The μ-ECT probe using GMR sensor enabled us to detect and distinguish between markers printed by conductive and magnetic inks. The feature of detecting signal was discussed among two kinds of markers and the difference in the phase was important from the distinction of markers. We built the experimental apparatus using the probe and confirmed experimentally that it was possible to classify two kinds of markers by the phase of pick-up signal.

Even if the visual appearance such as color and shape of a marker are the same, it is possible to detect and distinguish conductive and magnetic markers by their electromagnetic properties. The simultaneous use of two kinds of markers dramatically improves the reliability of marker security printed on a paper medium because of increased information.

References

1) AgIC Inc., http://agic.cc/ja/ (2015).
2) S. Yamada, K. Chomusuwan, Y. Fukuda, M. Iwahara,H. Wakiwaka, and S. Shoji, *IEEE Trans. on Magn.*, **40**, 4 (2004).
3) K. Chomusuwan, Y. Fukuda, S. Yamada, M. Iwahara, H. Wakiwaka, and S. Shoji, *J. Magn. Soc. JPN*, **4**, 1 (2004).
4) M. Cacciola, G. Megalo, D. Pelicano, and F.C. Morabino, *Sensors and Actuators A : Physical*, **167**, 1, 25 (2011).
5) K. Chomusuwan, S. Yamada, and M. Iwahara, *IEEE Sensors J.,* **7**, 5 (2007).
6) K. Chomusuwan, S. Yamada, and M. Iwahara, *IEEE Trans. on Magn.*, **43**, 6 (2007).
7) H. Murata, Y. Ikehata, and S. Yamada, *IEEJ Trans. on Electronics Information and System*, **134**, 5 (2014). [in Japanese]
8) T. Minamitani, S. Uraoka, and S. Yamada, *Digest of 2015 JIEE Annual Conference*, **2-115** (2015). [in Japanese]
9) T. Minamitani, S. Uraoka, and S. Yamada, *JIEE Technical Paper of Magnetic Meeting,* **MAG-14-139** (2014). [in Japanese]
10) R.L.Stoll, The analysis of eddy currents, Chp.2, Clarendon Press, Oxford (1974).

<Paper>

Fundamental Iron Loss Characteristics of Ring Cores Connected in Series and Parallel under Inverter Excitation

S. Odawara, and K. Fujisaki

Toyota Technological Institute, *Nagoya, Aichi, 468-8511, Japan*

When iron loss characteristics on an inverter excitation are evaluated by using multiple loads connected in series, they indicate lower iron losses compared with using the loads connected in parallel. It indicates that multiple loads should be connected in series to reduce the iron loss when the loads are excited by one inverter. This phenomenon is caused by semiconductor on-voltages changed by the connection method. This conclusion is introduced by an experimental evaluation using three ring cores made of electrical steel sheets (35H300). In addition, to corroborate the experimental results, a numerical analysis is carried out, in which both of characteristics of magnetic hysteresis and semiconductor are taken into account. Analysis results also indicate the same tendency as the experimental results.

1. Introduction

Utilization rate of electric equipment is increasing in modern society, because of its superior characteristics as controllability, high responsiveness, cleanness and reversibility. In addition, a motor drive system becomes possible to be applied to transportation system as not only automobile but also ship or airplane by power electronics technology.

Since arbitrary frequencies and voltages can be provided in high response by switching operation of inverter, it is possible to control rotation speeds of electrical motors easily. The electrical motors have cores made of magnetic materials such as electrical steel sheets. Therefore, they are excited magnetically with time-harmonics by an inverter for controlling frequencies and voltages. However, the characteristics of electrical steel sheets are determined by a sinusoidal excitation without time-harmonics according to domestic and international standards[1)-2)], and it is usually used for design of the electrical motors.

Many researchers have reported that the carrier harmonics in inverter excitation causes iron loss increase of electrical steel sheet[3)-5)]. In addition, it is revealed in our previous research that the iron loss characteristics are also affected by on-voltages of semiconductor in an inverter circuit: the shape of minor loops is changed by the amplitude of on-voltages and the iron loss is changed by them[6)-9)].

The on-voltages are changed by currents passing the semiconductor. Namely, the on-voltages depend on currents and voltages applied in load such as a motor. Therefore, when multiple loads are excited by using one inverter, the load-currents and the load-voltages are different from the case of single-load due to division of current and voltage. It indicates that the iron loss characteristics are affected by connection method of multiple loads.

A train drive system, in which one inverter drives multiple induction motors connected in parallel, is shown as an example of using multiple loads system[10)]. Moreover, in an electrical motor, the slot winding has an option of series-connection or parallel-connection. These connection methods are selected from a standpoint of controllability[11)-13)] or desired motor characteristics. However, in conventional investigations, iron loss characteristics have not been focused on in the connection methods. Therefore, the connection methods should be investigated from a standpoint of iron loss characteristics to reduce loss on driving system.

Consequently, as a fundamental investigation, the iron loss characteristics are measured by using multiple ring cores made of electrical steel sheets. They are connected in series or in parallel and excited by single-phase PWM (pulse width modulation) inverter. In this study, to obtain the difference by connection method clearly, three ring cores are used for the evaluation. In addition, to corroborate the experimental results, the numerical analysis is also carried out, in which both characteristics of semiconductor and magnetic material are taken into account[14)-16)].

2. Influence of on-voltages on Minor Loops

2.1 Single-load

First, the influence of on-voltages is described by using single-phase inverter shown in Fig. 1 and single-ring shown in Fig. 2(a). The specifications of one ring core are shown in Table I. V_{out} and I_{out} in Fig. 1 are the output-voltage and the output-current of the inverter. V_{on} in Fig. 1 is the on-voltage of semiconductor in the inverter circuit. V_{ring} and I_{ring} in Fig. 2 are the ring-voltage and the ring-current applied to one ring core. The single-phase inverter excitation has two modes: ON-mode and OFF-mode as shown in Fig. 3. The following circuit equations (1) and (2) are obtained from ON-mode and OFF-mode, respectively.

$$V_{dc} = V_s + V_{ring} + V_s, \tag{1}$$

$$0 = V_s + V_{ring} + V_f, \tag{2}$$

where V_s and V_d are the on-voltage of IGBT and diode. Therefore, the ring-voltages V_{ring} of ON-mode and OFF-mode are expressed as the following equations (3) and (4), respectively.

$$V_{ring} = V_{dc} \pm 2\,V_s, \tag{3}$$

$$V_{ring} = \pm(V_s + V_f). \tag{4}$$

"±" is decided by direction of current flow. For example, when the current flows through voltage source and IGBT 3 and ring and IGBT 2, "−" is selected in equation (3).

Magnetic field intensities H and magnetic flux densities B are calculated by the following equations:

$$H = \frac{N_1 I_{ring}}{l}, \tag{5}$$

$$B = \frac{1}{N_2 S} \int V_{ring}\,dt, \tag{6}$$

where N_1, N_2, l, and S are the primary winding number, the secondary winding number, the average magnetic-path length, and the cross-sectional area of the ring core, respectively. Strictly, the secondary voltage e should be used for calculating B because the voltage drop of the primary coil can be neglected. However, for easy explanation, it is assumed that the primary voltage V_{ring} is the same as the secondary voltage e because N_1 and N_2 are the same.

Fig. 4 shows B-H curve on an inverter excitation. The minor loops are observed and they cause the iron loss increase[6)-8)]. The minor loops are caused by the drop of magnetic flux density ΔB_{off}. ΔB_{off} is caused in OFF-mode of inverter excitation as follow:

$$\Delta B_{off} = \frac{1}{N_2 S} \int_{off} V_{ring}\,dt = \pm \frac{1}{N_2 S} \int_{off} (V_s + V_f)\,dt. \tag{7}$$

Equation (7) indicates that the minor loops become large when the large on-voltage applies to ring core, and it affects iron losses increase [6)-9)].
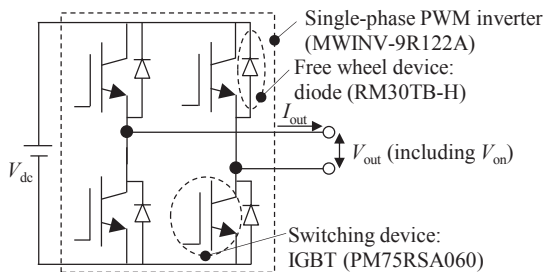

Fig. 1 Single-phase PWM inverter for exciting ring cores.

Table I Specifications of one ring core.

Material	35H300
Outside diameter	127 mm
Inside diameter	102 mm
Height	7 mm
Primary coil winding number	254 turns
Secondary coil winding number	254 turns

(a) Single-ring

(b) Series-connection

(c) Parallel-connection
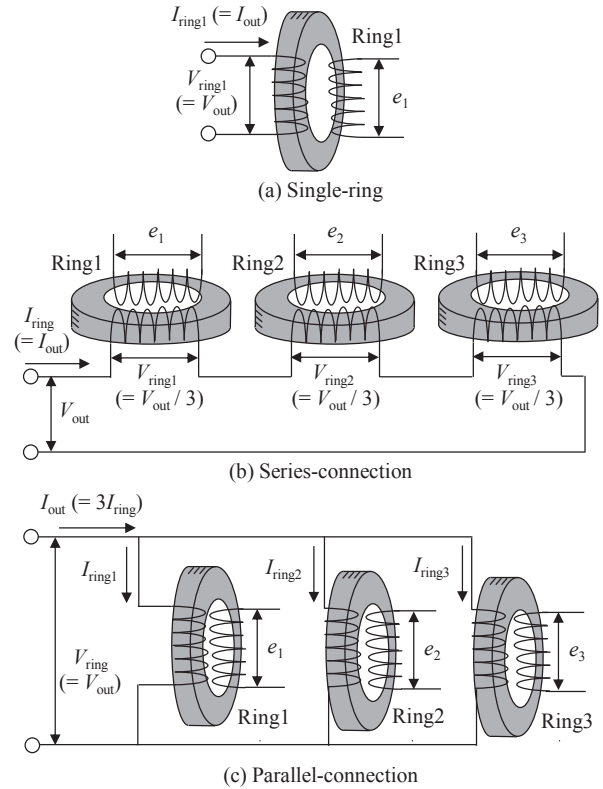
Fig. 2 Connections of ring cores.

(a) ON-mode (b) OFF-mode
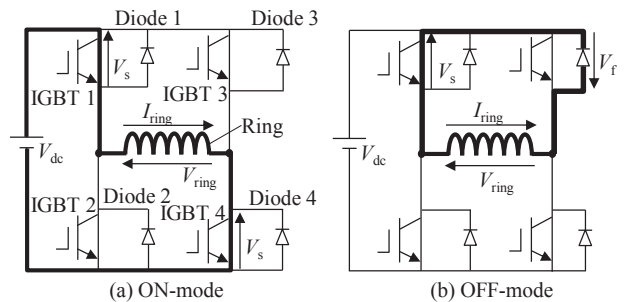
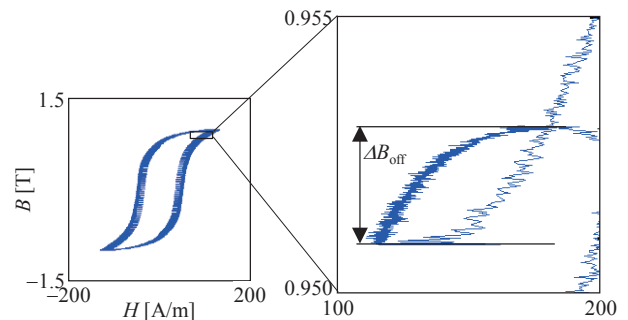**Fig. 3** Current flows in inverter circuit for both modes.

Fig. 4 B-H curve under PWM inverter excitation.

2.2 Three ring cores connected in series or in parallel

In series-connection shown in Fig. 2(b), the ring-voltage V_{ring} becomes a one-third of the output-voltage V_{out}. The ring-current I_{ring} should become the same as the case of single-ring when each ring core is excited under the same excitation conditions as single-ring. Since on-voltages V_{on} depends on I_{ring} (i.e. I_{out}), V_{on} included in V_{out} is also the same as the case of single-ring. Therefore, V_{on} applied to one ring core also becomes a one-third.

On the other hand, in parallel-connection shown in Fig. 2(c), the output-current I_{out} becomes triple of the ring-current I_{ring}. Therefore, V_{on} of parallel-connection becomes large compared with that of single-ring, because I_{out} flowing in the semiconductor is three times larger than that of single-ring. It causes changing the operating point in current-voltage (I-V) characteristics of semiconductor.

Thus, V_{on} applied to one ring core in series-connection becomes smaller than parallel-connection. It is expected that the iron losses in series-connection will become smaller than that in parallel-connection.

3. Experimental Investigation

3.1 Method for measurements

The three ring cores connected in series or in parallel are excited by single-phase inverter shown in Fig. 1 under the following conditions: fundamental frequency f_o is 50 Hz, modulation index m is 0.6, and carrier frequency f_c is changed from 1 kHz to 20 kHz. The applied DC voltage V_{dc} is set so that the maximum magnetic flux density B_{max} becomes 1 T in each ring core.

3.2 On-voltages on each connection

First, on-voltage V_{on} included in ring-voltage V_{ring} is evaluated to confirm an influence by difference of connection method. Fig. 5 shows output-current I_{out} and V_{ring1} waveforms of ring 1 on $f_c = 10$ kHz and the enlargement near the maximum I_{out}. V_{on} emerges as voltage protrusion from zero on OFF-mode as shown in Fig. 5(b).

In Fig. 5, it is confirmed that the on-voltages are changed by the series-connection and the parallel-connection. On the series-connection waveform shown in Fig. 5 (c), the on-voltage becomes about a one-third of on-voltage on single-ring due to voltage dividing.

On the other hand, the on-voltage on parallel-connection shown in Fig. 6 (d) is a little larger than that on single-ring, because I_{out} flowing in semiconductor becomes about three times larger than single-ring. It causes changing the operating point on I-V characteristics in semiconductor. These phenomena are described in detail in next analytical investigation chapter.

The experimental results indicate the phenomena according to the theory mentioned in section 2-2. Therefore, it is confirmed from the experiment that the on-voltages characteristics are changed by the series-connection and the parallel-connection.
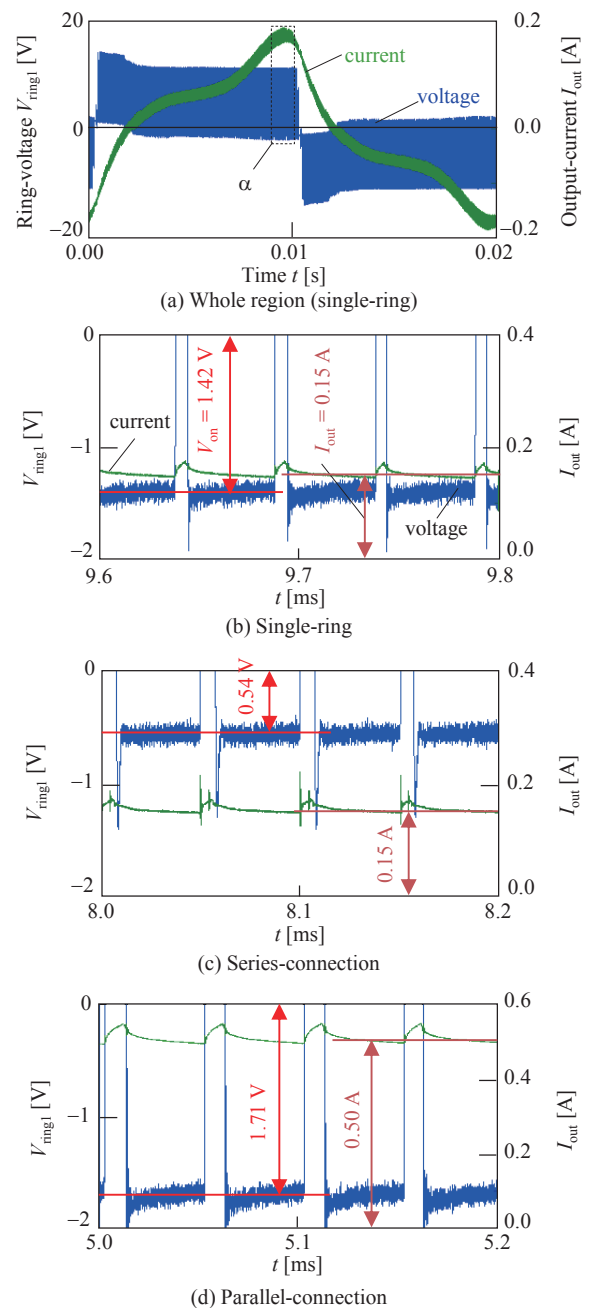

Fig. 5 Measured on-voltages from each connection ($f_c = 10$ kHz).

3.3 B-H curves

B-H curves are depicted from obtained B and H in the series-connection and the parallel-connection. Fig. 6 shows the measured B-H curves in ring 1 obtained from both connections on $f_c = 10$ kHz. It also shows minor loops near the maximum flux density. The minor loop of series-connection is smaller than that of parallel-connection, because the on-voltage of series-connection is small. The minor loop leads the iron loss increase because the iron loss is proportional to surface integral of B-H hysteresis curve and the surface integral is performed in addition on the minor loops. Therefore, it is expected that the iron loss becomes small in series-connection.
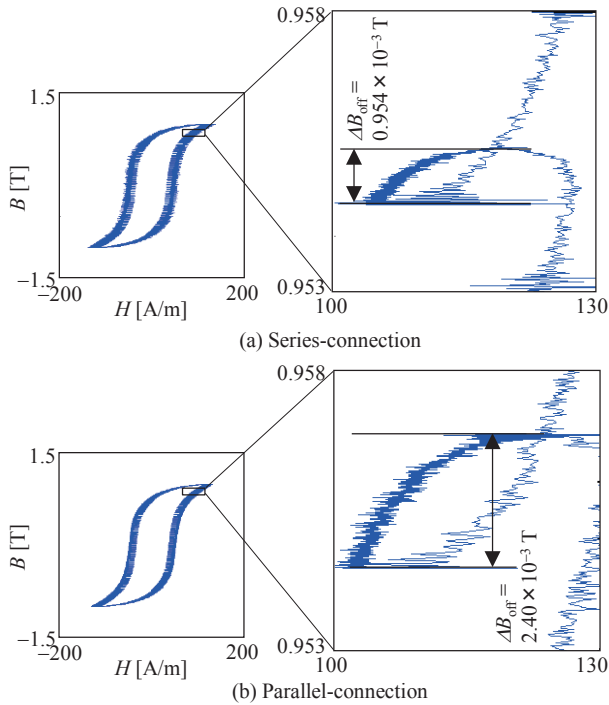
(a) Series-connection

(b) Parallel-connection

Fig. 6 Measured B-H curves in ring 1 (f_c = 10 kHz).

Table II Iron losses on each connection (f_c = 10 kHz).

$W_{fe}{}^*$ [W/kg]	Series connection	Parallel connection
Ring 1	1.14	1.18
Ring 2	1.14	1.19
Ring 3	1.14	1.18
Total	3.42	3.55

Fig. 7 Carrier frequency characteristics of total iron loss obtained from experiment.

3.4 Iron loss characteristics

Finally, the iron loss characteristics are evaluated in both connections. The iron loss is calculated by the following equation (8). In the measurement, it is difficult to set the maximum flux density B_{max} to 1 T strictly. Therefore, a normalization of iron loss on just B_{max} = 1 T is performed by using the following equation (9). In equation (9), the iron loss is assumed to be proportional to the square of magnetic flux density.

$$W_{fe} = \frac{f_o}{\rho} \int H dB , \qquad (8)$$

$$W_{fe}{}^* = W_{fe} \times 1^2 / B_{max}{}^2 , \qquad (9)$$

where ρ is the density of electrical steel sheet (= 7650 kg/m³) and superscript (*) means the normalized value.

Table II shows the iron losses obtained from each connection on f_c = 10 kHz. In Table II, it is indicated that there is no dispersion of three rings characteristics because the iron losses are the same as each other. The iron losses of series-connection are smaller than that of parallel-connection. The total iron loss of parallel-connection is about 3.8 % larger than series-connection.

To confirm the phenomenon, the iron losses are obtained by changing the carrier frequencies. Fig. 7 shows the carrier frequency characteristics of total iron loss on each connection. In each carrier frequency, the iron losses from series-connection are smaller than that from parallel-connection. The minimum peak indicated in Fig. 8 is caused by dead-time effect of inverter excitation. The dead-time makes additional applied voltage require in higher carrier frequency[17]. It makes additional current (i.e. additional H) and makes the loss increased.

4. Analytical Investigation

4.1 Method for analysis

A numerical analysis[15)-16)] is carried out to corroborate the phenomena obtained from the experiment. The numerical analysis can take into account both of semiconductor characteristics and magnetic hysteresis characteristics. The analysis is performed according to flowchart shown in Fig. 8[16)].

When the circuit analysis is carried out in process (v), on-voltages are calculated by using I-V characteristics. Fig. 9 shows the I-V characteristics of semiconductors used for this analysis. The operating points of the series-connection and the parallel-connection, which are mentioned in section 3-2, are also shown in Fig. 9. In Fig. 9, an approximation according to a quadratic expression is performed on region less than the current of 1 A, because it cannot be obtained from datasheets. V_{CE} and V_F correspond to the on-voltages of the IGBT and the diode, respectively.

When the magnetic analysis is carried out in process (iii), Play model[18)-19)] and Cauer's equivalent circuit[20)-21)] shown in Fig. 10 are used for considering magnetic hysteresis. The magnetic field intensity H is calculated by inputting the magnetic flux density B obtained from generated output-voltage in circuit analysis. In Cauer's circuit, v, i, L, and R_E correspond to dB/dt, H, the permeability, and the classical eddy-current loss, respectively. By solving the circuit equation, the following equations are obtained.

$$H^k(B^k) = H_1^k + H_2^k + H_3^k , \qquad (10)$$

$$R_E = \frac{12}{\kappa \sigma d^2} , \qquad (11)$$

$$H_2^k = C_1 H_3^k + H_2^{k-1} , \qquad (12)$$

$$H_3^k = \frac{1}{C_2}\{3(B^k - B^{k-1}) - 3R\Delta t H_2^{k-1}\} , \qquad (13)$$

$$C_1 = \frac{35}{3L'}R\Delta t , \qquad (14)$$

$$C_2 = R\Delta t(3C_1 + 10) \qquad (15)$$

where σ is the electric conductivity (= $1.92*10^6$ S/m), d is the thickness of electrical steel sheets (= 0.35 mm). κ is the anomaly factor and it is set to 2 according to Ref. (16). L' is linear inductance and it is set to 1.6 mH according to Ref. (16). The DC magnetic properties $H_{DC}(B)$ is obtained by scalar play model[18)-19)].

In this numerical analysis, influences of dead-time and rise time of the semiconductor are neglected for simplicity.

4.2 Analysis results

Fig. 10 shows analyzed on-voltages corresponding to Fig. 5. The on-voltage values is the almost same as experimental results shown in Fig. 5. Fig. 12 shows the analyzed hysteresis curves on the series-connection and the parallel-connection. The analysis results express not only the major loop but also the difference of minor loops sizes obtained from measurement shown in Fig. 6.

Fig. 13 shows the carrier frequency characteristics on total iron loss corresponding to Fig. 7. The analysis results indicate the same tendency as experimental results: the iron loss obtained from parallel-connection is larger than that from series-connection on each carrier frequency.
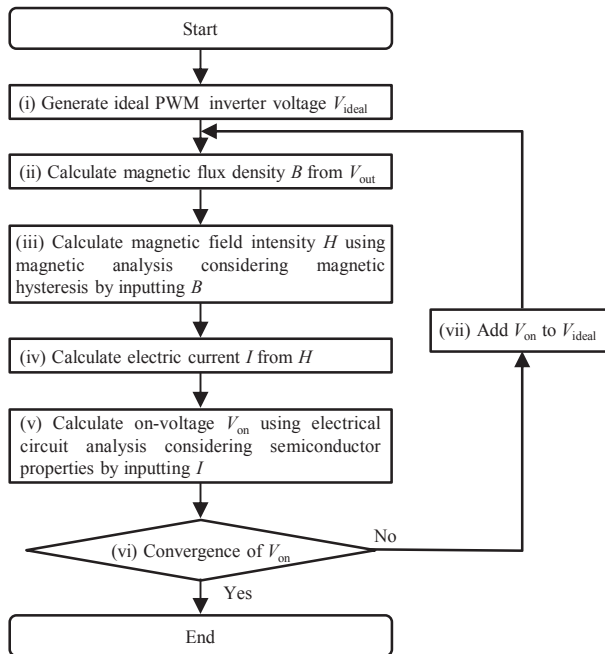
In this analysis, the dead-time effect is neglected for simplicity. Therefore, the minimum peak mentioned in Fig. 7 is not observed. Moreover, the analyzed difference of the parallel-connection and the series-connection is smaller than the experimental results. It is caused by dead-time effects. Dead-time makes additional current require on higher carrier frequency. Therefore, since additional current also becomes three times in parallel-connection, V_{on} is easy to be affected by the additional current. It causes the difference of analysis and experiment.
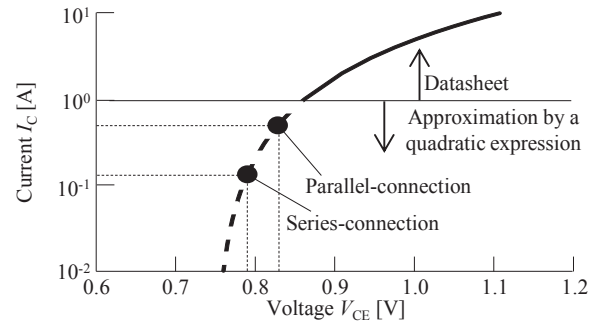
(a) Switching device (IGBT: PM75RSA060).
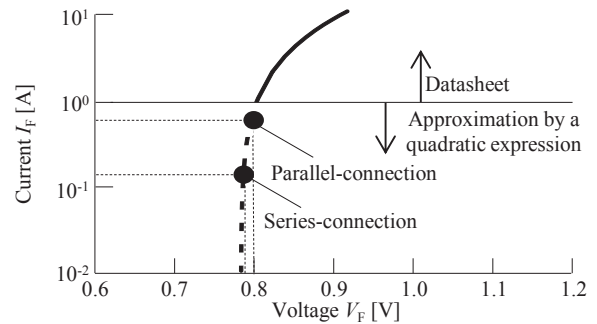
(b) Free wheel device (diode: RM30TB-H).

Fig. 9 I-V characteristics of power semiconductors and operating points on both connections.
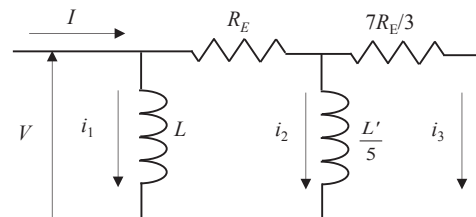
Fig. 10 Cauer's equivalent circuit to consider magnetic hysteresis characteristics.
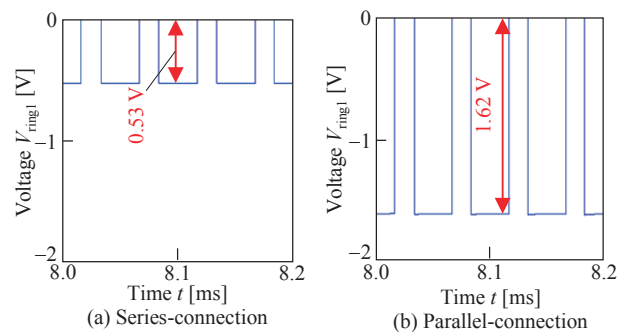

Fig.8 Flowchart of numerical calculation taking into account semiconductor characteristics and magnetic material[16)].

(a) Series-connection (b) Parallel-connection

Fig. 11 Analyzed on-voltages from each connection (f_c = 10 kHz).

(a) Series-connection
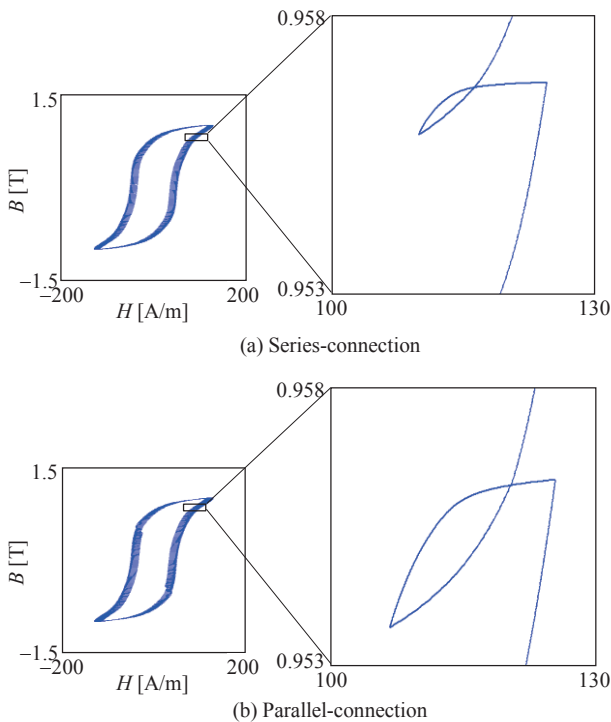

(b) Parallel-connection

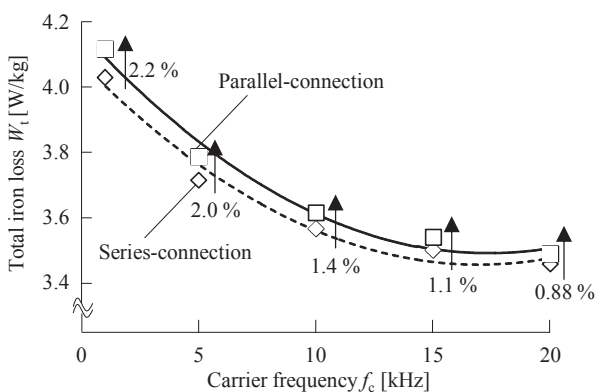**Fig. 12** Analyzed $B\text{-}H$ curves in ring 1 (f_c = 10 kHz).

Fig. 13 Carrier frequency characteristics of total iron loss obtained from numerical analysis.

5. Conclusion

The influence of series-connection and parallel-connection is evaluated from the standpoint of iron loss characteristics. The on-voltage, the $B\text{-}H$ curve, and the iron loss are obtained by measurement using three ring cores. Obtained results are shown as follows.

1) On-voltages of each ring core on series-connection become three times smaller than that on parallel-connection, because the voltage dividing of on-voltage is caused by series-connection.
2) Since on-voltage on series-connection is small, minor loops in magnetic hysteresis which is led by the on-voltage becomes smaller than parallel-connection.

3) Since minor loops of series-connection is small, iron loss on series-connection is smaller than parallel-connection.
4) These results are also corroborated by the numerical analysis taking into account both of the magnetic hysteresis property and the semiconductor property.

According to these results, in order to reduce the iron losses, multiple loads should be connected in series when they are driven by one inverter.

References

1) International Electrotechnical Commission, 60404-3, Second edition, 1992.
2) Japanese Industrial Standard, C2556, 1996.
3) A. Boglietti, P. Ferraris, M. Lazzari, and F. Profumo: *IEEE Trans. Magn.*, vol. **27**, no. 6, pp.5334-5336, 1991.
4) M. Kawabe, T. Nomiyama, A. Shiozaki, H. Kaihara, N. Takahashi, M. Nakano: *IEEE Trans. Magn.*, vol. **48**, no. 11, pp. 3458–3461, 2012.
5) H. Matsumori, T. Shimizu, K. Takano, and H Ishii: *Energy Conversion Congress and Exposition (ECCE)*, 2012.
6) K. Fujisaki, and S. Liu: *Journal of Applied Physics*, **115**, 17A321, 2014.
7) D. Kayamori, K. Fujisaki: *IEEE Power Electronics and Drive Systems (PEDS)*, 9034, 2013.
8) S. Odawara, D. Kayamori, and K. Fujisaki: *IEEJ Trans. Industry Applications,* vol.**134**, no.7, pp. 649-655, 2014, (in Japanese).
9) S. Odawara, D. Kayamori, and K. Fujisaki: *IEEJ Trans. Fundamentals and Materials*, vol.**135**, no.7, pp. 385-390, 2015, (in Japanese).
10) T. Hasebe, and H. Yamamoto: *Toshiba review*, vol. **61**, no. 9, 2006 (in Japanese).
11) T. Nagano, Y. Nakajima, Y. Noge, and J. Itoh: *IEEJ Industry Applications Society Conference,* L2177B, 2012 (in Japanese).
12) K. Matsuse, H. Kawai, Y. Kouno, and J. Oikawa: *IEEE Trans. Industry Applications,* vol. **40**, no. 1, pp. 153-161, 2004.
13) N. Urasaki, T. Senjyu, and K. Uezato: *IEEE Trans. Energy Conversion,* vol. **19**, no. 2, pp. 265-270, 2004.
14) S. Odawara, K. Fujisaki, and F. Ikeda: *IEEE Trans. Magn.*, vol. **50**, no. 11, article #: 7201004, 2014.
15) S. Odawara, K. Fujisaki, and T. Matsuo: *Energy Conversion Congress and Exposition (ECCE)*, P2105, 2014.
16) S. Odawara, K.Fujisaki, T. Matsuo, and Y. Shindo: *IEEJ Trans. Industry Applications,* vol. **135**, no. 12, 2015 (in Japanese).
17) T. Tanaka, S. Koga, R. Kogi, S. Odawara, and K. Fujisaki: *IEEJ Trans. Industry Applications,* vol. **136**, no. 2, 2015 (in Japanese) (in press).
18) S. Bobbio, G. Miano, C. Serpico and C. Visone: *IEEE Trans. Magn.*, vol. **33**, no. 6, pp. 4417-4426, 1997.
19) T. Matsuo and M. Shimasaki: *IEEE Trans. Magn.*, vol. **41**, no. 10, pp. 3112-3114, 2005.
20) J. H. Krah : *IEEE Trans. Magn*, vol. **41**, no. 5, pp. 1444-1447, 2005.
21) Y. Shindo, O. Noro: *IEEJ Trans. FM*, vol.**134**, no.4, pp. 173- 181, (2014).

<Paper>

Iron Loss Calculation for Concentric-Winding Type Three-Phase Variable Inductor based on Reluctance Network Analysis

Kenji Nakamura, Yuta Yamada, Takashi Ohinata*, Kenji Arimatsu*,
Takehiko Kojima**, Makoto Yamada**, Ryohei Matsumoto**,
Masaya Takiguchi**, and Osamu Ichinokura

Graduate School of Engineering, Tohoku University, *6-6-05 Aoba Aramaki Aoba-ku, Sendai 980-8579, Japan*
*Tohoku Electric Power Co., Inc., *1-7-1 Honcho Aoba-ku, Sendai 980-8550, Japan*
**Fuji Electric Co., Inc., *1-11-2 Osaki Shinagawa-ku, Tokyo 141-0032, Japan*

A variable inductor consisting of just a magnetic core and primary dc and secondary ac windings, is able to control effective inductance of the secondary ac winding linearly and continuously by the primary dc current due to magnetic saturation effect. Therefore, it can be applied as a var compensator in electric power systems. The variable inductor has desirable features such as simple and robust structure, low cost, and high reliability. In a previous paper, a novel concentric-winding type three-phase variable inductor was proposed. It was demonstrated in experiments that the proposed variable inductor has good controllability and low distortion current. This paper presents a method for calculating iron loss of the proposed variable inductor based on reluctance network analysis (RNA). The validity of the proposed method is demonstrated through a comparison with measured values.

Key words: three-phase variable inductor, concentric-winding, iron loss, reluctance network analysis (RNA)

1. Introduction

In electric power systems, line voltage stabilization is one of the important subjects because renewable and distributed power sources such as wind-turbine and photovoltaic power generations are being introduced in large quantities. In order to regulate the line voltage, the semiconductor power converters such as a static var compensator (SVC) and a static synchronous compensator (STATCOM) have been introduced [1], [2]. These apparatuses, however, have some problems including harmonic current, electromagnetic interference (EMI), and high cost.

A variable inductor consists of only a magnetic core and primary dc and secondary ac windings [3], but can control effective inductance of the secondary ac winding linearly and continuously by the primary dc current due to magnetic saturation effect. Thus, it can be used as a var compensator by combining with a power capacitor [4]. The variable inductor has simple and robust structure, high reliability, and low cost. These features are advantages for applications in electric power systems. Several kinds of variable inductors have been proposed. However, all the previously proposed variable inductors have a single-phase structure. Hence, at least three variable inductors are required for the var compensation in electric power systems.

To resolve the above problem, a three-phase variable inductor was presented in a previous paper [5]. It has only one laminated-core in which three-phase secondary ac windings are installed together. The previous three-phase variable inductor demonstrated good controllability and low distortion current, but the winding space factor was low since the primary dc windings must be placed on the ring yoke.

To improve the winding space factor, a novel concentric-winding type three-phase variable inductor was proposed [6], [7]. It has primary dc and secondary ac windings which are concentrically wound on each leg. It was indicated that the reactive power per weight of the proposed variable inductor is about 1.6 times larger than that of the previous one, namely, the weight of the proposed variable inductor can be reduced by 40% [8].

This paper presents an iron loss calculation of the proposed variable inductor based on reluctance network analysis (RNA). The establishment of the iron loss calculation method is indispensable for the optimum design of the var compensator. The usefulness of the proposed method is proved by comparing with measured values.

2. Basic configuration and operating principle of concentric-winding type three-phase variable inductor

Fig. 1 illustrates a basic configuration of a concentric-winding type three-phase variable inductor, which consists of six legs, two ring yokes, and primary dc
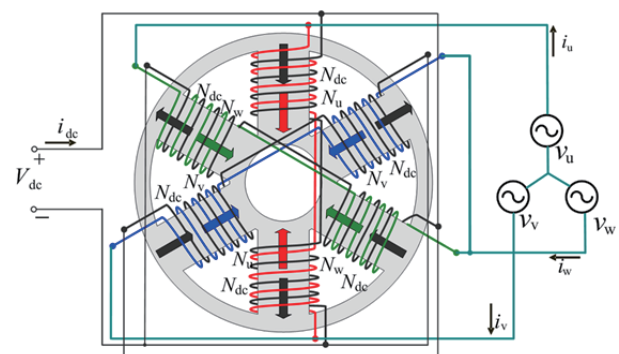

Fig. 1. Basic configuration of a concentric-winding type three-phase variable inductor.

and secondary ac windings. The secondary ac windings N_u, N_v, N_w are coiled around each couple of legs on the straight line, respectively. These windings are connected in delta, and to the three-phase ac voltage source. On the other hand, each primary dc winding N_{dc} is concentrically wound on the leg where the secondary ac winding is coiled around, and a couple of the primary dc windings on the straight line is connected in series to cancel the induced voltages caused by the secondary ac fluxes.

3. Iron loss calculation for concentric-winding type three-phase variable inductor

Fig. 2 shows the specifications of a trial 4.0 kVA concentric-winding type three-phase variable inductor. The core material is non-oriented silicon steel with a thickness of 0.35 mm. The number of turns of the primary dc winding N_{dc} is 114, and the secondary ac windings N_u, N_v, N_w are 208 each. The rated capacity and voltage are 4.0 kVA and 200 V so that it can be handled in the laboratory. Fig. 3 indicates an appearance of the trial concentric-winding type three-phase variable inductor.
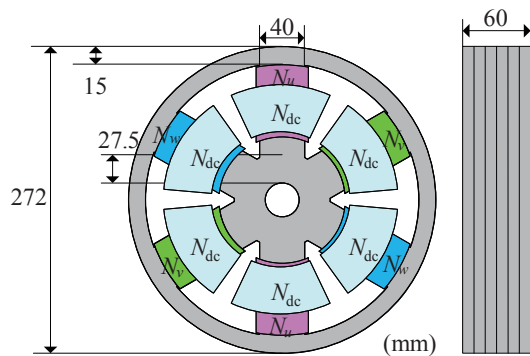
Rated capacity	4.0 kVA
Rated voltage	200 V
Frequency	50 Hz
Primary dc winding: N_{dc}	114 turns x 6, 0.164 Ω/coil
Secondary ac winding: N_u, N_v, N_w	208 turns x 6, 0.604 Ω/coil
Winding space factor	43.9%
Core material	NGO with 0.35 mm

Fig. 2. Specifications of a trial 4.0 kVA concentric-winding type three-phase variable inductor.
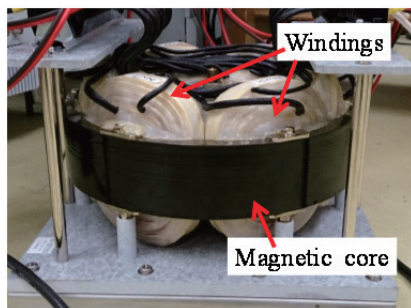

Fig. 3. Appearance of the trial 4.0 kVA concentric-winding type three-phase variable inductor.

To calculate the iron loss of the variable inductor, three-dimensional (3-D) RNA is employed because its analytical model is simple, the calculation speed and accuracy are high, and the coupled analysis is readily performed.
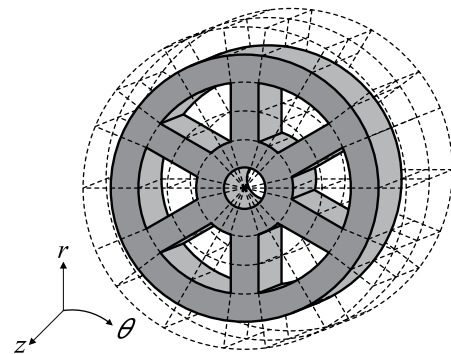
First, the three-phase laminated-core is divided into multiple elements as shown in Fig. 4(a). To take leakage flux into consideration, the surrounding space of the core is also divided. The divided elements can be expressed in a 3-D unit magnetic circuit shown in Fig. 4(b). When the 3-D unit magnetic circuit is in the core region, the reluctances R_{mr} and $R_{m\theta}$ express the magnetic nonlinearity, and the magnetic inductances R'_r and R'_θ represent the iron loss of the core. These elements can be obtained as follows.

When considering the iron loss, a relationship between the magnetic field H and the flux density B can be given by [9]

$$H = \alpha_1 B + \alpha_m B^m + \beta_1 \frac{dB}{dt} + \beta_n \left(\frac{dB}{dt}\right)^n. \quad (1)$$

The first and second terms of (1) denote the magnetic nonlinearity, and the third and fourth terms express the iron loss.

The coefficients α_1 and α_m are determined by a B-H curve of core material shown in Fig. 5(a), while the coefficients β_1 and β_n are obtained from a core loss curve shown in Fig. 5(b), which includes hysteresis and eddy current losses in the core. These coefficients are $m = 13$, $\alpha_1 = 106$, $\alpha_{13} = 6.3$, $n = 9$, $\beta_1 = 0.14$, and $\beta_9 = 2.0\times10^{-26}$, respectively.
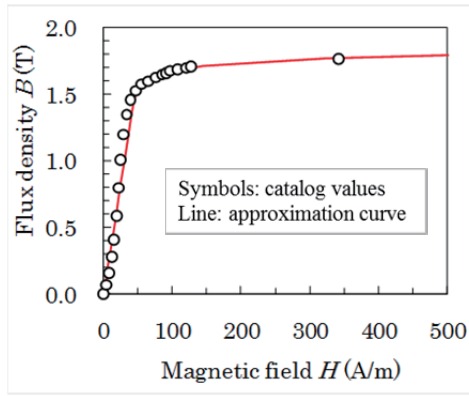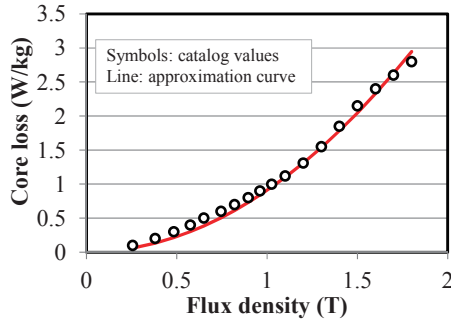

(a) Core division
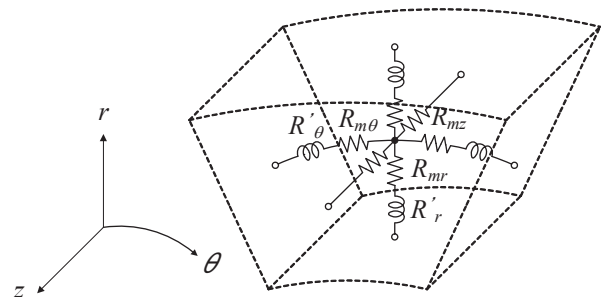
(b) 3D unit magnetic circuit

Fig. 4. Three-dimensional RNA model of the three-phase laminated-core.

(a) B-H curve

(b) Core loss curve

Fig. 5. B-H curve and core loss curve of the core material.

From (1), a relationship between the magnetomotive force (MMF) f and the flux ϕ is given by

$$f = Hl$$

$$= R_m \phi + R' \frac{d\phi}{dt}$$

$$= \left(\frac{\alpha_1 l}{S} + \frac{\alpha_m l}{S^m} \phi^{m-1} \right) \phi + \left\{ \frac{\beta_1 l}{S} + \frac{\beta_n l}{S^n} \left(\frac{d\phi}{dt} \right)^{n-1} \right\} \frac{d\phi}{dt} \ , (2)$$

where the magnetic path length and the cross section of each divided element are l and S, respectively. The reluctances and the magnetic inductances in the 3-D unit magnetic circuit can be determined by (2).

On the other hand, the reluctance R_{mz} in the z-axis direction should be determined considering a laminated structure of the core. Apparent permeability in the z-axis μ_e is given by

$$\frac{1}{\mu_e} = \frac{d_f}{\mu_s} + \frac{1 - d_f}{\mu_0}$$

$$\cong \frac{1 - d_f}{\mu_0} \ , \qquad (3)$$

where the vacuum and core permeability are μ_0 and μ_s, and the space factor of the laminated silicon steel core is d_f, respectively. Accordingly, R_{mz} is obtained as a linear reluctance from (3).

On the other hand, when the unit magnetic circuit is in the surrounding space, the linear reluctances R_{mr}, $R_{m\theta}$, R_{mz} are obtained from the dimensions of each divided element and the vacuum permeability μ_0, while the magnetic inductances R'_r, R'_θ are zero.
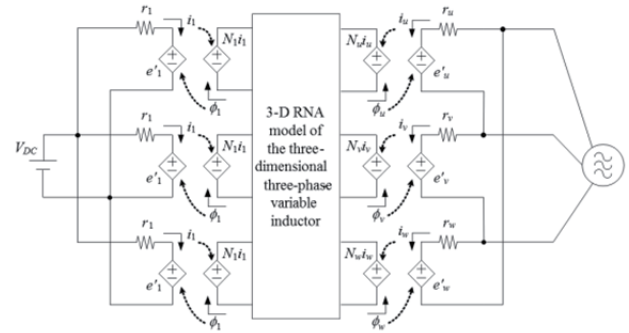

Fig. 6. Electric- and magnetic-coupled model of the concentric-winding type three-phase variable inductor.
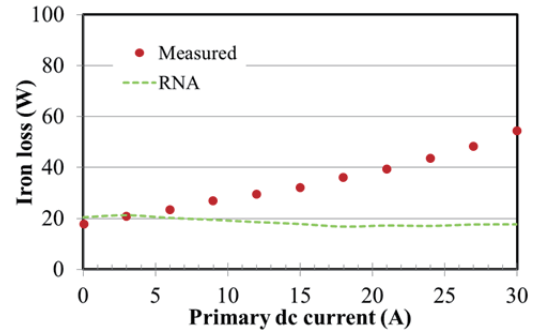

Fig. 7. Measured and calculated iron losses of the concentric-winding type three-phase variable inductor.

Finally, when the RNA model obtained in the way described above is coupled with the external electric circuits as shown in Fig. 6, the characteristics of the variable inductor can be calculated by a general purpose circuit simulator SPICE [10].

Fig. 7 shows the measured and calculated iron losses of the concentric-winding type three-phase variable inductor. Both values are in good agreement when a primary dc current is 0 A. Contrary to this, the error increases as the primary dc current becomes large. The reason is that the RNA model shown in Fig. 4 is able to consider only the iron loss caused by the flux flowing in the r- and θ-directions, which is parallel with the laminated silicon steel. On the other hand, the eddy current loss caused by the leakage flux flowing in the z-axis direction, which is perpendicular to the laminated silicon steel, is neglected

4. RNA model considering eddy currents on laminated silicon steel

In general, the eddy currents on the laminated silicon steel are distributed in a complicated manner. To take this into consideration in RNA, the following assumption is applied [11]: The distribution of the eddy currents is based on the division of the RNA model as shown in Fig. 8, and the eddy current flows uniformly in each element.

To express the eddy current on the laminated silicon steel in the RNA model, the 3-D unit magnetic circuit and the eddy current circuit are combined as shown in Fig. 9. In the figure, the leakage flux ϕ_z gives the induced

voltage e_z. From the induced voltage e_z and the resistance R_{ed}, the eddy current i_{ed} can be obtained, which gives the MMF in the 3-D unit magnetic circuit. In practice, all the eddy current circuits are connected with each other as shown in Fig. 10 to consider the current interaction between the adjacent elements.
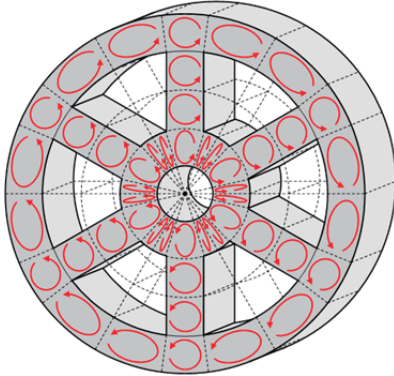

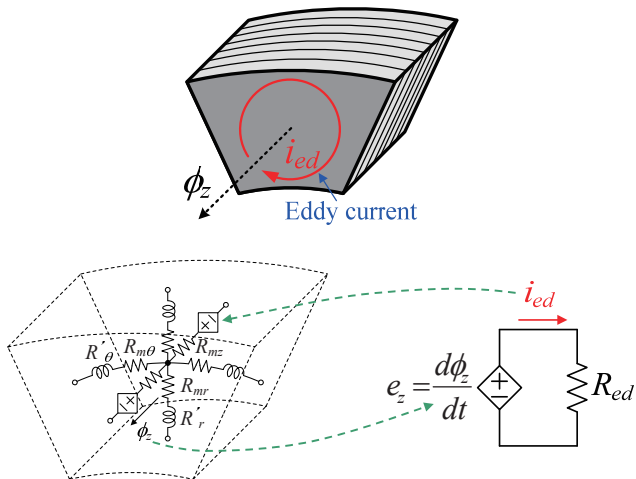**Fig. 8.** Distribution of the eddy currents in the RNA model.

Fig. 9. 3-D unit magnetic circuit combined with the eddy current circuit.
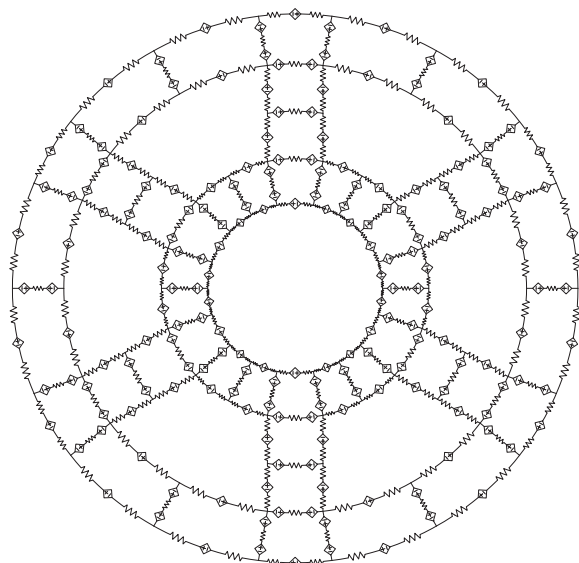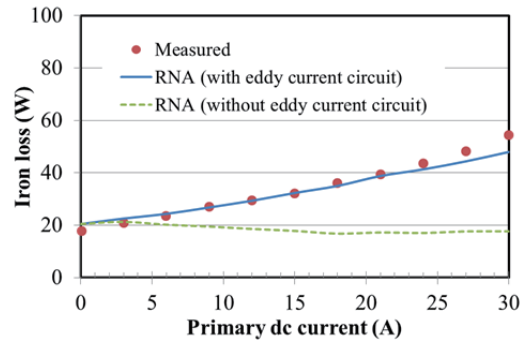

Fig. 10. Eddy current network model.

Fig. 11. Comparison of the measured and calculated iron losses of the concentric-winding type three-phase variable inductor.

Fig. 11 shows the comparison of the measured and calculated iron losses of the concentric-winding type three-phase variable inductor. In the figure, the symbols show the measured values and the solid line indicates the calculated ones. In addition, the broken line represents the calculated values when the eddy current on the laminated silicon steel is ignored. The figure clearly indicates that the calculated values agree well with the measured ones.

5. Conclusion

This paper presented a method for calculating iron loss of the concentric-winding type three-phase variable inductor based on RNA.

It was clear that the eddy currents on the laminated silicon steel must be considered in order to estimate the iron loss of the concentric-winding type three-phase variable inductor. The usefulness of the proposed method was proved by comparing with the measured values.

References

1) L. Gyugyi, *IEEE Trans. Ind. Applicat.*, **IA-15**, 521 (1979).
2) S. Mori, K. Matsuno, T. Hasegawa, S. Ohnishi, M. Takeda, M. Seto, S. Murakami, and F. Ishiguro, *IEEE Trans. Power Sys.*, **8**, 371 (1993).
3) S. D. Wanlass, C. L. Wanlass, and L. K. Wanlass, *IEEE Wescon Tech. Papers*, **12**, part 2 (1968).
4) O. Ichinokura , T. Tajima, and T. Jinzenji, *IEEE Trans. Magn.*, **29**, 3225 (1993).
5) K. Nakamura, S. Hisada, K. Arimatsu, T. Ohinata, K. Sakamoto, and O. Ichinokura, *IEEE Trans. Magn.*, **44**, 4107 (2008).
6) K. Nakamura, K. Honma, T. Ohinata, K. Arimatsu, T. Shirasaki, and O. Ichinokura, *J. Magn. Soc. Jpn.*, **38**, 174 (2014).
7) K. Nakamura, K. Honma, T. Ohinata, K. Arimatsu, and O. Ichinokura, *Journal of Applied Physics*, **117**, 17D523 (2015).
8) K. Nakamura, K. Honma, T. Ohinata, K. Arimatsu, T. Kojima, M. Yamada, R. Matsumoto, M. Takiguchi, and O. Ichinokura, *IEEE Trans. Magnetics*, **51**, 8402104 (2015).
9) K. Tajima, O. Ichinokura, A. Kaga, and Y. Anazawa, *J. Magn. Soc. Jpn.*, **19**, 553 (1995) (in Japanese).
10) K. Tajima, A. Kaga, and O. Ichinokura, *T. IEE Japan*, **117-A**, 155 (1997) (in Japanese).
11) K. Nakamura, T. Tomonaga, S. Akatsuka, T. Ohinata, K. Minazawa, and O. Ichinokura, *J. Magn. Soc. Jpn.*, **30**, 273 (2006).

<Paper>

Center-Constricted Magnetic Core-Coil Structures for Resonant Wireless Power Transfer

Hirotaka Oshima and Satoshi Shimokawa

Fujitsu Laboratories Ltd., *10-1 Morinosato-Wakamiya, Atsugi 243-0197, Japan*

Magnetic core-coil structures for resonant wireless power transfer are proposed to enhance power transfer efficiency between opposed flat coils. A central region in the direction perpendicular to the plane of a magnetic core plate is constricted with a coil wound closely around the region to increase the figure of merit kQ, the product of the coupling coefficient k and the quality factor Q. The proposed effect is analyzed in terms of a magnetic circuit model. Electromagnetic field simulation of the systems determines the equivalent circuit parameters and confirms quantitatively the increase in kQ by the center-constricted structures.

Key words: wireless power transfer, magnetic core, resonant coil, coupling coefficient, quality factor, magnetic circuit, electromagnetic field simulation

1. Introduction

Wireless power transfer using resonant coils [1,2] has been attracting considerable attention as a new route to efficient electrical power transfer at a distance without cable. Power transfer efficiency between the coils is determined by the figure of merit kQ[3], the product of the coupling coefficient between the coils (k) and the quality factor of the coils (Q).

For higher efficiency, a soft magnetic core with high permeability can be inserted into a coil to increase kQ. It is particularly effective for long and narrow solenoidal coils, since the self-inductance (L) and hence Q of such coils are proportional to the permeability of the core [4]. A thin plate core inserted in a flat spiral coil, on the other hand, does not yield such a significant effect due to the demagnetization effect. When the demagnetization factor (N_d) of a thin plate core is close to unity, L of a flat coil with the plate core can be approximated as $L = L_0/N_d$, where L_0 is the inductance of an air-core coil with the same dimensions [4]. In this case, L is close to L_0 and independent of the core permeability. Flat spiral coils are often adopted for mobile devices and electric vehicles, and generally used in opposed configurations. Large bulky cores to reduce N_d are, therefore, not practically applicable due to the limited dimensions of the equipment.

Here, we propose center-constricted magnetic core-coil structures that can enhance the efficiency of resonant wireless power transfer without increasing thickness of a plate core inserted in a flat coil. In the following section, the proposed structures are described. The mechanism of the kQ enhancement is explained in terms of a magnetic circuit model in section 3. The effect is confirmed by numerical electromagnetic field simulation by analyzing lumped parameters for an equivalent circuit in section 4. Simulation taking magnetic core loss into account is also performed. The results are discussed in section 5, and the paper is concluded in section 6.

2. Center-constricted magnetic core-coil structures

2.1 Power transfer efficiency and kQ

Before describing the proposed magnetic core-coil structures, the relationship between power transfer efficiency (η) and kQ in a resonant wireless power transfer system is briefly noted below.

The figure of merit kQ of a two resonant coil system [Fig. 1(a)] can be defined as $kQ = k(Q_1 Q_2)^{1/2}$, where k is the coupling coefficient and Q_1, Q_2 are the quality factors of the resonant coils. By using the self-inductance L_1, L_2, and the mutual-inductance M_{12}, k can be written as $k = M_{12}/(L_1 L_2)^{1/2}$. Q_1, Q_2 of the coils are given by $Q_1 = \omega L_1/R_1$, $Q_2 = \omega L_2/R_2$, respectively. Here, ω is the resonant angular frequency and R_1, R_2 are the electric resistance of the coils. From these equations, kQ of the coils can be written as,

$$kQ = \omega M_{12}/(R_1 R_2)^{1/2}. \tag{1}$$

When electric power is transferred between the coils, a power source and a load are directly attached to [5] or inductively coupled with [6,7] one and the other, respectively. In general, η depends on the impedance of the load [8]. When the load impedance is optimally adjusted, the maximum η can be described as a function of kQ and given by [9],

$$\eta = (kQ)^2/[1+\{1+(kQ)^2\}^{1/2}]^2. \tag{2}$$

In Fig. 1(b), we plot the maximum η as a function of kQ. It is a monotonically increasing function: the larger kQ gives the larger η. Consequently, enhancement of kQ is immediately effective in increasing the optimum efficiency of a resonant wireless power transfer system.

2.2 Magnetic core structures for a flat coil

We propose here a magnetic core structure for a flat coil to enhance kQ without increasing thickness of a plate core attached to the coil. A schematic example of the structure is shown in Fig. 2(a). A soft magnetic material with high permeability is used for the core. The structure has a constricted region in the center in the direction perpendicular to the plane. A coil is wound
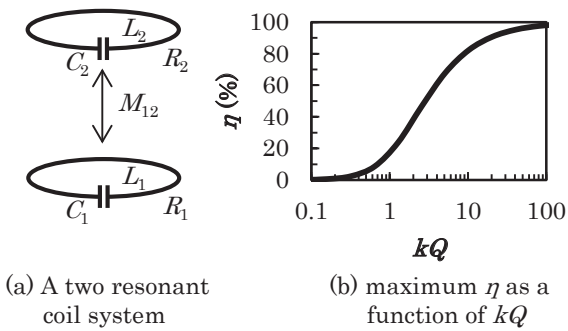
(a) A two resonant coil system

(b) maximum η as a function of kQ

Fig. 1 (a) A two resonant coil system for resonant wireless power transfer. (b) Maximum η as a function of kQ.

closely around the constricted region. A capacitor is connected in series with the coil for resonance (not shown in Fig. 2 for simplicity). As shown in Fig. 2(b), the central region with a thickness y has a diameter D_c, whereas the outer (upper and lower) regions with a thickness x have a diameter D_0.

As mentioned in section 1, a flat coil with a thin plate magnetic core ($N_d \sim 1$) inside the coil only shows kQ similar to an air-core coil with the same diameter. Compared to those coils with the diameter D_0, the proposed magnetic core-coil structure shows larger kQ, as will be described below. Note that we use throughout

(a) center-constricted magnetic core-coil structure
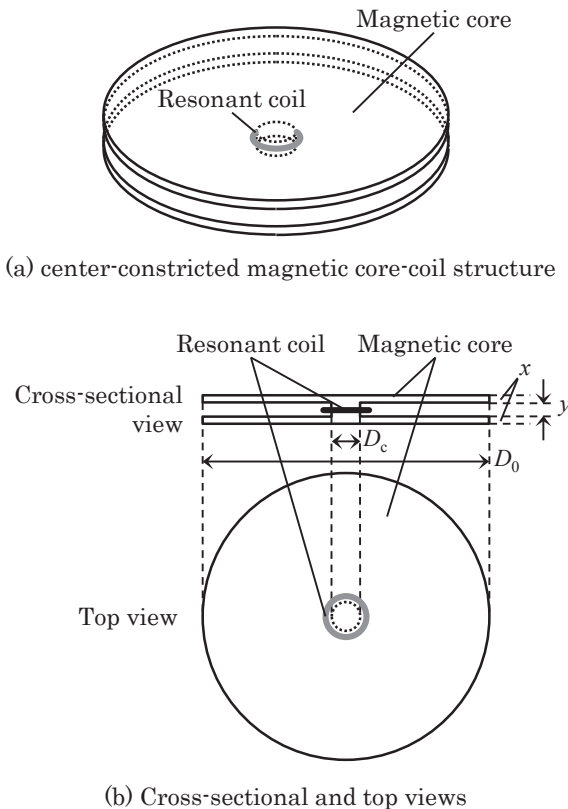

(b) Cross-sectional and top views

Fig. 2 (a) A schematic of a center-constricted magnetic core-coil structure, (b) its cross-sectional and top views. A capacitor for resonance is not shown for simplicity.

the paper symmetric circular coils and cores to make the following analysis clear and simple, although similar effect could be obtained in other shapes.

3. Mechanism of kQ enhancement

3.1 Effect of the center constriction

The essential effect of the center constriction described above can be explained briefly as follows. Suppose one of the resonant coils has the proposed center-constricted magnetic core-coil structure with the parameter $\beta = D_0/D_c$ that represents the degree of the center constriction. Equation (1) signifies that kQ is equal to the ratio of ωM_{12} to $(R_1 R_2)^{1/2}$. As will be shown below, both of the quantities are decreasing functions of β. The point is that, when β increases, relative decrease in $R^{1/2}$ is much larger than that in M_{12}. This leads to a corresponding increase in kQ with increase in β. In the next section, we illustrate why the mutual-inductance M_{12} does not decline as much as the coil resistance $R^{1/2}$ when increasing the constriction β in terms of a magnetic circuit model.

3.2 Magnetic circuit model

Mutual-inductance between coils is proportional to the interlinkage magnetic flux. Let us suppose that one of the coils is and air-core coil with an area S_0, and that the interlinkage magnetic flux passing through the air-core coil is Φ_0. We then consider replacement of the air-core coil with our center-constricted magnetic core-coil structure having the same projected area S_0 and the constricted core area $S_C = S_0/\beta^2$, as shown in Fig. 3(a). Here the inner diameter of the resonant coil is assumed to be the same as that of the constricted core, and the coil wire width is ignored. In such a case, distribution of the magnetic flux can be analyzed with a magnetic circuit model in analogy with electric current in an electric circuit [10),11)]. In the proposed structure, magnetic resistance (reluctance) of the center region can be modeled as a parallel circuit of the magnetic resistance of the constricted core and the surrounding air, as illustrated in Fig. 3(b). Assuming that all the magnetic flux Φ_0 passes through either the constricted core or the air surrounding the core between the upper and lower plate cores, magnetic resistance of the constricted core and the air are given by $R_C = l/\mu_C S_C$ and $R_a = l/\mu_0(S_0 - S_C)$, respectively, where l is the length of the path and μ_C is the magnetic permeability of the core. As the coil of the structure is wound closely around the constricted core, the interlinkage magnetic flux passing through the coil (Φ_C) can be described as,

$$\Phi_C = \mu_C S_C \Phi_0/[\mu_0(S_0 - S_C) + \mu_C S_C]$$
$$= \mu_r \Phi_0/(\mu_r + \beta^2 - 1), \qquad (3)$$

where μ_r is the relative permeability of the core material ($\mu_C = \mu_r \mu_0$). Since the mutual-inductance is proportional to the interlinkage magnetic flux, as mentioned above, the mutual-inductance of the proposed structure (M_C) is given by,

$$M_C = \mu_r M_0/(\mu_r + \beta^2 - 1), \qquad (4)$$

where M_0 is the mutual-inductance of the air-core coil. For example, when the relative permeability $\mu_r = 1000$

and the constriction $\beta = 10$, M_C is estimated to be $0.91 M_0$. This means that the mutual-inductance would be more than 90% even when the area of the coil is reduced to 1% of the original one.

On the other hand, the electric resistance of the coil (R_C) is considered to be proportional to the coil length. R_C is, therefore, inversely proportional to β. Note that the core loss effect is neglected here. Simulation including the core loss will be shown below in section 5.

From the above results, when one of the air-core coils is replaced with a center-constricted magnetic core-coil structure, kQ of the system can be written as,

$$kQ = \omega M_C / (R_1 R_C)^{1/2}$$
$$= \mu_r \beta^{1/2} k_0 Q_0 / (\mu_r + \beta^2 - 1), \qquad (5)$$

where $k_0 Q_0$ is the kQ before the replacement. By substituting $\mu_r = 1000$ and $\beta = 10$ again in equation (5), we obtain $kQ = 2.9 k_0 Q_0$. In that condition, about three times larger kQ is expected by this new structure. The function $f(\mu_r, \beta) = \mu_r \beta^{1/2} k_0 Q_0 / (\mu_r + \beta^2 - 1)$ can thus be defined as the coefficient of enhancement. We plot in Fig. 4 the coefficient of enhancement f as a function of β for various μ_r. When μ_r is close to unity, the constriction only gives rise to the degradation in f. For larger μ_r, on the other hand, the constriction works effectively for the enhancement and the f becomes several times larger than those without the constriction. We also found that there exists the most effective β (β_{max}) for each large μ_r.

Fig. 4 The coefficient of enhancement $f(\mu_r, \beta)$ as a function of β for various μ_r.

4. Electromagnetic field simulation

4.1 Magnetic field distribution

To confirm the effect of the proposed structure, numerical electromagnetic field simulation has been performed. Lumped parameters (such as inductance and resistance) for an equivalent circuit are directly derived from the field distribution to calculate kQ [12]. Note that nonuniform current distribution in coils due to the skin effect and the proximity effect is explicitly considered in the simulation. We should also note that our previous simulations for various resonant wireless power transfer systems [13-15] have shown good agreement with experiments.

An example of spatial distribution of the magnetic field H and magnetic flux density B is given in Fig. 5. These figures show a cross section of the system: the amplitude is illustrated by the gradation, and the lines represent a snapshot of magnetic flux. In this example, the upper coil is the proposed center-constricted magnetic core-coil structure, and the lower one is an air-core coil having the same outer diameter for comparison. The outer (upper and lower) core plates have the diameter D_0 of 100 mm and the thickness x of 5 mm. The center cnstricted region has the diameter D_c of $D_0/10$ ($\beta = 10$) and the thickness y of 10 mm. A single-turn coil with the wire width of 1 mm and thickness of 0.1 mm is used throughout the paper for both of the air-core and magnetic-core coils to clarify the effect. The inner radius of the magnetic-core coil is set to be 1 mm larger than that of the center constricted region of the core to avoid the large proximity effect. The frequency is 100 kHz and μ_r is set to be 1000.

As described in section 3.2, the concentration of magnetic flux in the center constricted region of the core is necessary for the kQ enhancement. Fig. 5(b) shows that the magnetic flux indeed concentrates in the constriction and mostly passes through the upper coil, which suggests the effectiveness of the proposed center-constricted magnetic core-coil structure. In this calculation, the electric current in the lower air-core coil in Fig. 5 was set to be 1.0 A as a typical example, and

(a) Interlinkage magnetic flux
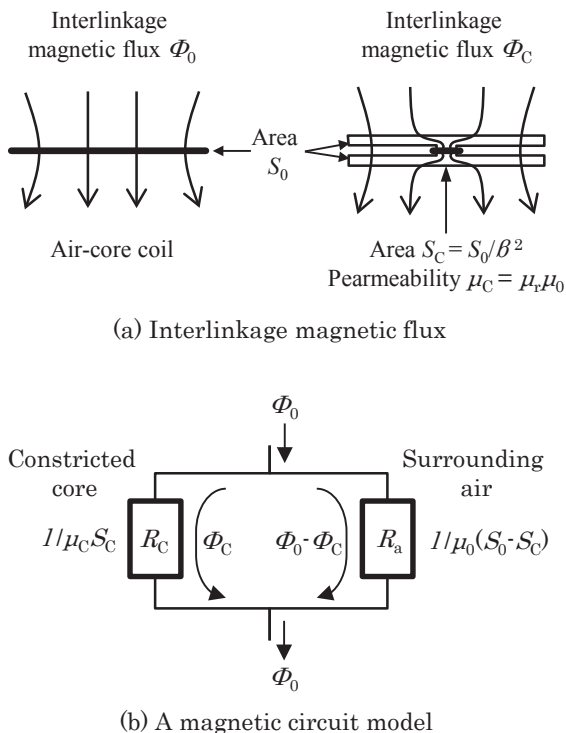

(b) A magnetic circuit model

Fig. 3 (a) Interlinkage magnetic flux through an air-core coil (left) and a center-constricted magnetic core-coil structure with the same projected area (right), (b) A magnetic circuit model for interlinkage magnetic flux through the center-constricted magnetic core-coil structure.
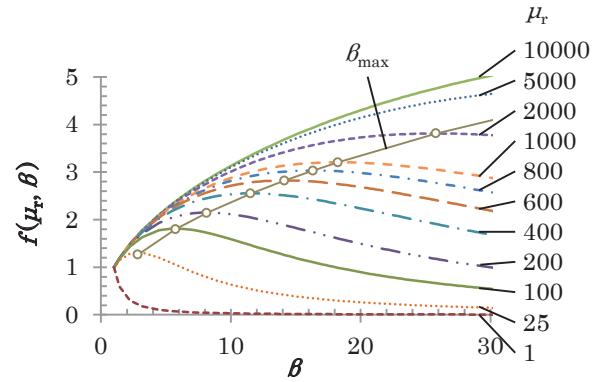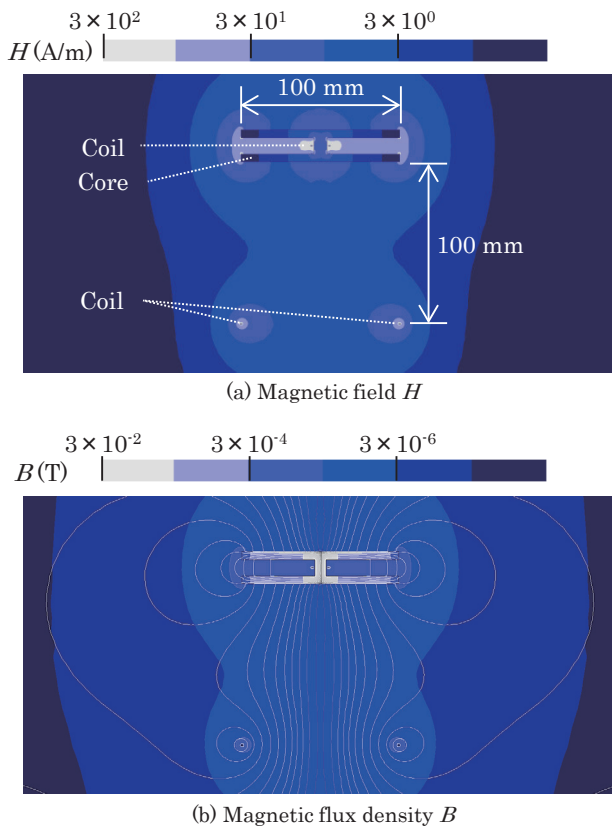
(a) Magnetic field H

(b) Magnetic flux density B

Fig. 5 An example of spatial distribution of (a) magnetic field H and (b) magnetic flux density B around the system. The gradations show log-scale contour plots of H and B divided into six levels. The lines in (b) show a snapshot of magnetic flux.

the current in the upper one in that condition was 2.2 A. It should be noted that the maximum B in the magnetic core in Fig. 5(b) is well below 2×10^{-2} T, which is an order smaller than a typical value of saturation magnetic flux density of ferrite core material.

4.2 Center-constriction effect on kQ

Fig. 6 presents kQ as a function of β for various μ_r, calculated from the lumped circuit parameters deduced from the electromagnetic field simulation. The dimensions of the center-constricted magnetic core-coil structure are identical to those described in section 4.1. An air-core coil with the diameter of 500 mm is used here for the counterpart to yield a nearly homogeneous field as schematically illustrated in Fig. 3(a). Fig. 6(a) shows the calculated kQ values, whereas Fig. 6(b) shows the kQ normalized by the values at $\beta = 1$ (with no constriction) to clarify the constriction effect. Note that the normalized kQ corresponds to the coefficient of enhancement $f(\mu_r, \beta)$ defined in section 3.2.

The results in Fig. 6 clearly show that kQ can be increased by increasing β provided that μ_r is large enough. When μ_r is rather small, on the other hand, kQ decreases monotonically. It should also be mentioned that the maximum (normalized) kQ depends on μ_r and
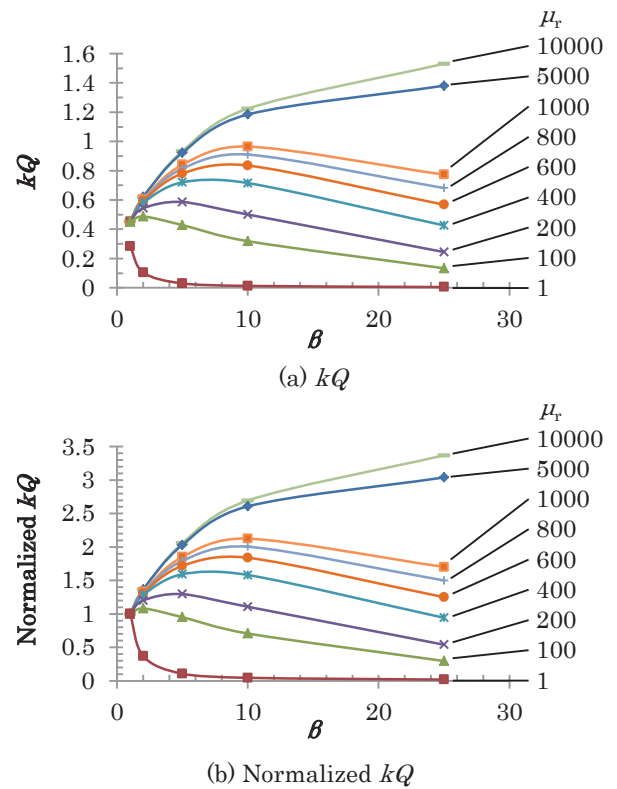

(a) kQ

(b) Normalized kQ

Fig. 6 (a) Simulated kQ as a function of β for various μ_r. (b) kQ normalized by the values at $\beta = 1$ (with no constriction).

the corresponding β increases with the increment of μ_r.

4.3 Comparison with the magnetic circuit model

We can find here that the results in Fig. 6(b) described in section 4.2 show β-dependent behavior qualitatively similar to those in Fig. 4 derived from the magnetic circuit model. The consistency suggests the validity of the simple model in section 3.2 to understand the basic physics of the kQ enhancement effect.

Further quantitative comparison, however, reveals that the maximum enhancement by the center constriction for each μ_r calculated by the above simulation is from 60% to 70% of the values obtained from the magnetic circuit model. It is probably due to magnetic flux leakage near the angulated constriction and the sharp outer edges of the core. In Fig. 7, we show coil resistance R_1 of the proposed structure and mutual-inductance M_{12}, obtained in the simulation and normalized by the values at $\beta = 1$. R_1 is indeed almost inversely proportional as expected in section 3.1, whereas M_{12} is somewhat smaller than expected from equation (4) for the coefficient of enhancement. The results suggest the existence of magnetic flux leakage larger than predicted by the magnetic circuit model. A closer look at R_1 also reveals that R_1 is slightly larger than the $1/\beta$ line for large β. This is probably due to the small gap between the coil and the core to avoid the proximity effect (as noted in section 4.1), which makes the diameter of the coil slightly larger than the core and
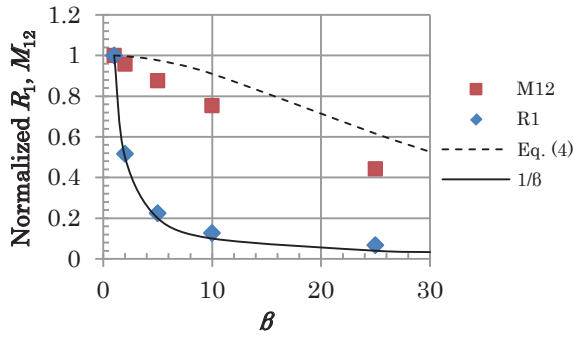
Fig. 7 Normalized R_1 and M_{12} as a function of β for $\mu_r = 1000$. Solid and dashed lines show $1/\beta$ and equation (4), respectively.
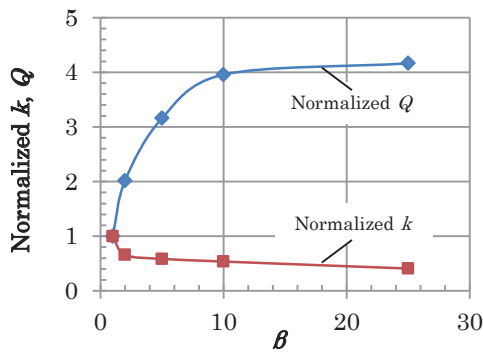

Fig. 8 Normalized k and Q as a function of β for $\mu_r = 1000$.

gives rise to increase in R_1 for large β.

It is also important to see the β-dependence of k and Q individually for comprehensive understanding of the effect. Fig. 8 shows normalized k and Q as a function of β. The results exemplify that, when β increases, k decreases to a certain extent whereas the increase in Q is large enough to outweigh the decrease in k. In other words, the center constriction degrades the coupling between the coils to some extent, but it concomitantly amplifies the resonant response of the coil considerably and consequently leads to the enhancement of their product kQ.

4.4 Application to both of the coils

All the studies shown above have dealt with a combination of a center-constricted magnetic core-coil structure and an air-core coil. It is to clarify the kQ enhancement effect by the proposed structure and better understand the underlying mechanism by comparing them with the magnetic circuit model. It should be added here, however, that the application of the structures to both of the coils (transmitter and receiver) is naturally more effective for the kQ enhancement.

We have confirmed by simulation that the effect by the center constriction is simply multiplied when it is applied to both of the coils. We first calculated β-dependence of the normalized kQ between a
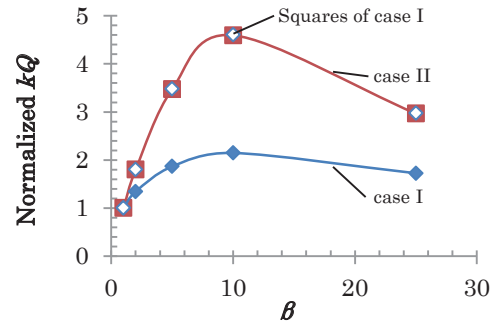

Fig. 9 kQ normalized by the values at $\beta = 1$ as a function of β for case I (a center-constricted magnetic core-coil structure and an air-core coil) and case II (two center-constricted magnetic core-coil structures) for $\mu_r = 1000$. The squares of the results of case I are also shown for comparison.

center-constricted magnetic core-coil structure and an air-core coil with the same outer diameter (case I). The dimensions of the center-constricted magnetic core-coil structure are identical to those described in sections 4.1 – 4.3 and Figs. 6 – 8. The pair shown in Fig. 5 is an example of case I. We then calculated the normalized kQ between the two center-constricted magnetic core-coil structures of the same dimensions for various β (case II). We found that the latter is exactly the square of the former for all the same β. The results for $\mu_r = 1000$ are shown in Fig. 9.

The results can be simply explained as follows. As elucidated in section 4.3, the center constriction of the magnetic core-coil structure leads to some decrease in k and large increase in Q between the coils (and resultant increase in the product kQ). The effect is independent of a type of the opposite coil. Consequently, the amplification of the normalized kQ is multiplied when we replace both of the coils to the center-constricted magnetic core-coil structures.

5. Core loss effect

Magnetic material has, in general, complex magnetic permeability: the imaginary part of permeability is related to the dissipation of energy. We have ignored it in all the simulations discussed above, partly because it is usually small at used frequencies for conventional magnetic core material such as ferrites, and partly because the ideal case should be examined first to make the effect clear and to compare the results with the magnetic circuit model. The loss tangent ($\tan\delta$) is an index of the energy loss and defined as the ratio of the imaginary part to the real part of permeability, where δ is the angle in a complex plane. Technically, it is non-zero even in ferrites. To investigate the core loss effect, therefore, we executed electromagnetic field simulation including $\tan\delta$ of magnetic material [13),15)].

In Fig. 10, we show β-dependence of kQ normalized by the values at $\beta = 1$ for various $\tan\delta$ for $\mu_r = 1000$ and
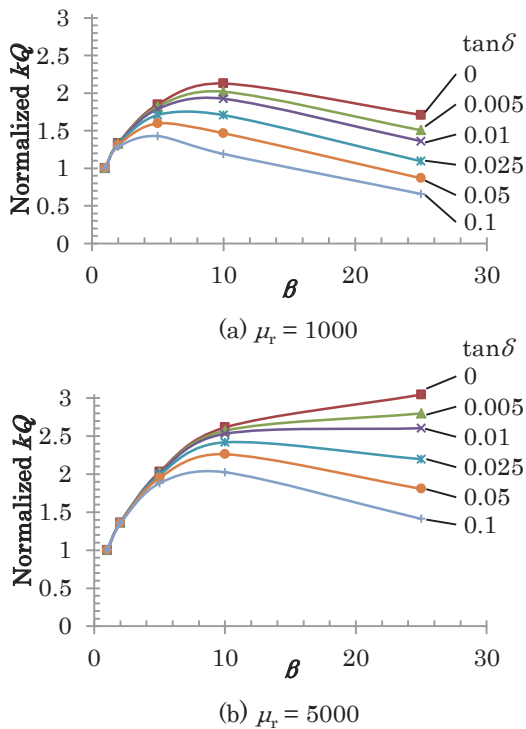
(a) $\mu_r = 1000$

(b) $\mu_r = 5000$

Fig. 10 kQ normalized by the values at $\beta = 1$ as a function of β for various $\tan\delta$. (a) $\mu_r = 1000$, (b) $\mu_r = 5000$.

5000. The core-coil system is identical to that employed in section 4.2. Consequently, the results for $\tan\delta = 0$ in Fig. 10(a) and 10(b) correspond to the results in Fig. 6(b) for $\mu_r = 1000$ and 5000, respectively. As shown in the figures, the increase in $\tan\delta$ in principle leads to the degradation of the kQ enhancement. The energy loss caused by $\tan\delta$ gives rise to increase in the effective electric resistance of the coil and resultant decrease in Q. We have confirmed, however, that the kQ enhancement effect is still significant for $\tan\delta \sim 0.01$, which is a typical value for standard ferrite material [16].

Additionally, we refer to the core loss factors. In this simulation we represented the core loss by homogeneous $\tan\delta$ due to magnetic hysteresis of core material, which would be appropriate for ferrites. At higher frequencies (typically above MHz in ferrites), however, the core loss due to displacement currents may also become innegligible, particularly for large cores [17]. In such cases, the dielectric effect should also be taken into account in simulation.

6. Conclusion

We have proposed center-constricted magnetic core-coil structures for opposed flat coils for resonant wireless power transfer. We derived the figure of merit kQ of the coil systems from electromagnetic field simulation by calculating lumped circuit parameters. We have demonstrated that the application of the proposed structures can enhance kQ without increasing the thickness of magnetic cores. The underlying mechanism of the effect can be understood by considering the corresponding magnetic circuit model. The quantitative difference between the results of the simulation and the model analysis is probably due to the simplistic design of the proposed core structures that gives rise to some undesirable leakage of magnetic flux from the wound coils. It suggests that there still is much room for improvement. We have also found that the enhancement effect is basically similar for multi-turn coils. However, the proximity effect, the skin effect, and the dimensions permitted for the coils make the determination of optimal designs more complicated. Further investigation is, therefore, needed to develop the most effective core-coil structures. We believe that the proposed structures are particularly effective for mobile devices as well as electric vehicles, which require efficient power supply but have little space for them. Studies from the perspective of magnetics would help improve the performance of such systems.

References

1) A. Kurs, A. Karalis, R. Moffatt, J. D. Joannopoulos, P. Fisher, and M. Soljačić: *Science*, **317**, 83 (2007).
2) T. Takura, Y. Ota, K. Kato, F. Sato, H. Matsuki, T. Sato, and T. Nonaka: *J. Magn. Soc. Jpn.*, **35**, 132 (2011).
3) A. Karalis, J. D. Joannopoulos, and M. Soljačić: *Ann. Phys.*, **323**, 34 (2008).
4) K. Shirakawa, H. Kurata, J. Toriu, H. Matsuki, and K. Murakami: *IEEE Trans. Magn.*, **27**, 5432 (1991).
5) Z. N. Low, R. A. Chinga, R. Tseng, and J. Lin: *IEEE Trans. Ind. Electron.*, **56**, 1801 (2009).
6) B. L. Cannon, J. F. Hoburg, D. D. Stancil, and S. C. Goldstein: *IEEE Trans. Power Electron.*, **24**, 1819 (2009).
7) A. P. Sample, D. A. Meyer, and J. R. Smith: *IEEE Trans. Ind. Electron.*, **58**, 544 (2011).
8) I. Awai: *IEICE Electron. Express*, **10**, 20132008 (2013).
9) M. Zargham and P. G. Gulak: *IEEE Trans. Biomed. Circuits Syst.*, **6**, 228 (2012).
10) C. J. Carpenter: *Proc. IEE,* **115**, 1503 (1968).
11) S. Chikazumi: Physics of Ferromagnetism, p.17 (Oxford Univ. Press, New York, 1997).
12) S. Shimokawa, H. Kawano, K. Matsui, A. Uchida, and M. Taguchi: *2011 IEEE MTT-S International Microwave Workshop Series on Innovative Wireless Power Transmission: Technologies, Systems, and Applications (IMWS),* 219 (2011).
13) H. Kawano, S. Shimokawa, A. Uchida, K. Matsui, K. Ozaki, and M. Taguchi: *IEICE Technical Report*, WPT2011-15 (2011) (in Japanese).
14) A. Uchida, S. Shimokawa, H. Kawano, K. Ozaki, K. Matsui, and M. Taguchi: *IET Microwaves, Antennas and Propagation,* **8**, 498 (2014).
15) A. Uchida, S. Shimokawa, K. Matsui, H. Kawano, K. Ozaki, and H. Oshima: *IEICE Technical Report*, WPT2014-42 (2014) (in Japanese).
16) See, for example, FDK standard power material 6H series: http://www.fdk.com/cyber-e/pdf/FP-FPE001.pdf (As of Jan. 04, 2016).
17) H. Saotome and Y. Sakaki: *IEEE Trans. Magn.* **33**. 728 (1997).

Notice for Photocopying

If you wish to photocopy any work of this publication, you have to get permission from the following organization to which licensing of copyright clearance is delegated by the copyright owner.

〈All users except those in USA〉
Japan Academic Association for Copyright Clearance, Inc.〔JAACC〕
6–41 Akasaka 9-chome, Minato-ku, Tokyo 107–0052 Japan
Phone 81–3–3475–5618　FAX 81–3–3475–5619　E-mail: info@jaacc.jp

〈Users in USA〉
Copyright Clearance Center, Inc.
222 Rosewood Drive, Danvers, MA01923 USA
Phone 1–978–750–8400　FAX 1–978–646–8600

複写をされる方へ

本会は下記協会に複写に関する権利委託をしていますので，本誌に掲載された著作物を複写したい方は，同協会より許諾を受けて複写して下さい．但し（社）日本複写権センター（同協会より権利を再委託）と包括複写許諾契約を締結されている企業の社員による社内利用目的の複写はその必要はありません．（社外頒布用の複写は許諾が必要です．）
権利委託先：一般社団法人学術著作権協会
　　　　　　〒107–0052 東京都港区赤坂9–6–41　乃木坂ビル
　　　　　　電話（03）3475–5618　FAX（03）3475–5619　E-mail: info@jaacc.jp
なお，著作者の転載・翻訳のような，複写以外の許諾は，学術著作権協会では扱っていませんので，直接本会へご連絡ください．